Segregation-induced fingering instabilities in granular free-surface flows

M. J. Woodhouse[1]†‡, A. R. Thornton[2], C. G. Johnson[1]‡, B. P. Kokelaar[3] and J. M. N. T. Gray[1]

[1] School of Mathematics and Manchester Centre for Nonlinear Dynamics, University of Manchester, Oxford Road, Manchester M13 9PL, UK

[2] Department of Applied Mathematics and Department of Mechanical Engineering, University of Twente, 7500 AE Enschede, The Netherlands

[3] Department of Geology and Geophysics, University of Liverpool, 4 Brownlow Street, Liverpool L69 3GP, UK

Particle-size segregation can have a significant feedback on the bulk motion of granular avalanches when the larger grains experience greater resistance to motion than the fine grains. When such segregation-mobility feedback effects occur the flow may form digitate lobate fingers or spontaneously self-channelize to form lateral levees that enhance run-out distance. This is particularly important in geophysical mass flows, such as pyroclastic currents, snow avalanches and debris flows, where run-out distance is of crucial importance in hazards assessment. A model for finger formation in a bidisperse granular avalanche is developed by coupling a depth-averaged description of the preferential transport of large particles towards the front with an established avalanche model. The coupling is achieved through a concentration-dependent friction coefficient, which results in a system of non-strictly hyperbolic equations. We compute numerical solutions to the flow of a bidisperse mixture of small mobile particles and larger more resistive grains down an inclined chute. The numerical results demonstrate that our model is able to describe the formation of a front rich in large particles, the instability of this front and the subsequent evolution of elongated fingers bounded by large-rich lateral levees, as observed in small-scale laboratory experiments. However, our numerical results are grid dependent, with the number of fingers increasing as the numerical resolution is increased. We investigate this pathology by examining the linear stability of a steady uniform flow, which shows that arbitrarily small wavelength perturbations grow exponentially quickly. Furthermore, we find that on a curve in parameter space the growth rate is unbounded above as the wavelength of perturbations is decreased and so the system of equations on this curve is ill-posed. This indicates that the model captures the physical mechanisms that drive the instability, but additional dissipation mechanisms, such as those considered in the realm of flow rheology, are required to set the length scale of the fingers that develop.

Key words: granular media, instability, shallow water flows

---

† Email address for correspondence: mark.woodhouse@bristol.ac.uk

‡ Current address: School of Mathematics, University of Bristol, University Walk, Bristol BS8 1TW, UK.

1. Introduction

Flows of granular materials, such as rockfalls, pyroclastic density currents, debris flows and snow slab avalanches, occur frequently in the natural environment and can be enormously destructive. The ability to predict the distance to which these flows travel is crucial for the mitigation of their threat. Accurate hazard assessment and planning strategies for minimizing the impact of these events can be greatly enhanced by physical models that are able to reproduce key features of these flows. While there has been significant progress in our understanding of the motion of granular materials, existing models are unable to describe all aspects of these hazardous flows. In particular, experimental observations of fingering instabilities (Pouliquen, Delour & Savage 1997; Pouliquen & Vallance 1999; Phillips *et al.* 2006; Goujon, Dalloz-Dubrujeaud & Thomas 2007, see also figure 1) and field studies (e.g. Pierson 1986; Iverson & Vallance 2001; Branney & Kokelaar 2002; Iverson 2003; Lube *et al.* 2007) have shown particle-size segregation significantly affects the behaviour of natural granular flows, particularly in the formation of levees. However, there have been very few attempts to include particle-size segregation in avalanche models.

Particle-size segregation, where a mixture of grains of differing sizes separate into distinct classes during flow, can occur through several mechanisms (see e.g. Cooke, Stephens & Bridgwater 1976; Ottino & Khakhar 2000). For dense granular avalanches, where the solids volume fraction is close to the random close packing fraction and where enduring particle contacts are the primary mechanism for particle interactions (Forterre & Pouliquen 2008), kinetic sieving and squeeze expulsion (Middleton 1970; Savage & Lun 1988) dominate. This results in a segregation of large particles upwards (i.e. against gravity) towards the free surface of the avalanching material, while smaller particles accumulate towards the base of the flow.

The first model of kinetic sieving and squeeze expulsion was developed by Savage & Lun (1988) from a statistical argument on the distribution of void space within a shearing granular assemblage. This model was able to predict steady-state size distributions for simple chute flows of bidisperse granular materials. Dolgunin & Ukolov (1995) used an *ad hoc* phenomenological argument to obtain a similar model that included a diffusive term to account for the remixing that occurs in faster flows. Recently, Gray & Thornton (2005), Thornton, Gray & Hogg (2006), Gray & Chugunov (2006) and Gray & Ancey (2011) derived a model of particle-size segregation using the techniques of mixture theory (see e.g. Truesdell 1984; Morland 1992). The structure of the resulting equation, which describes the evolution of the small particle concentration $\phi(x, y, z, t) \in [0, 1]$, is similar to those obtained by Savage & Lun (1988) and Dolgunin & Ukolov (1995). Experimental investigations of particle-size segregation in dense, slow granular flows on inclined chutes (Savage & Lun 1988; Vallance & Savage 2000; Wiederseiner *et al.* 2011) and in an annular shear cell (Golick & Daniels 2009; May *et al.* 2010) have shown that vertical size segregation is very efficient and that zones of nearly 100 % small and large particles are formed, which are often separated by a diffuse transition. Wiederseiner *et al.* (2011) obtained high-spatial-resolution observations of particle-size segregation during the flow down an inclined chute and demonstrated the evolving particle distribution predicted by the Gray & Chugunov (2006) model is consistent with the experimental observations. Vallance & Savage (2000) investigated the effect of adding a background fluid and showed that the density of the fluid has a large effect on segregation, completely suppressing the segregation in the case where fluid and particle densities are matched. The effect of the interstitial fluid has been incorporated into a segregation model that includes an inviscid interstitial fluid (Thornton *et al.* 2006).
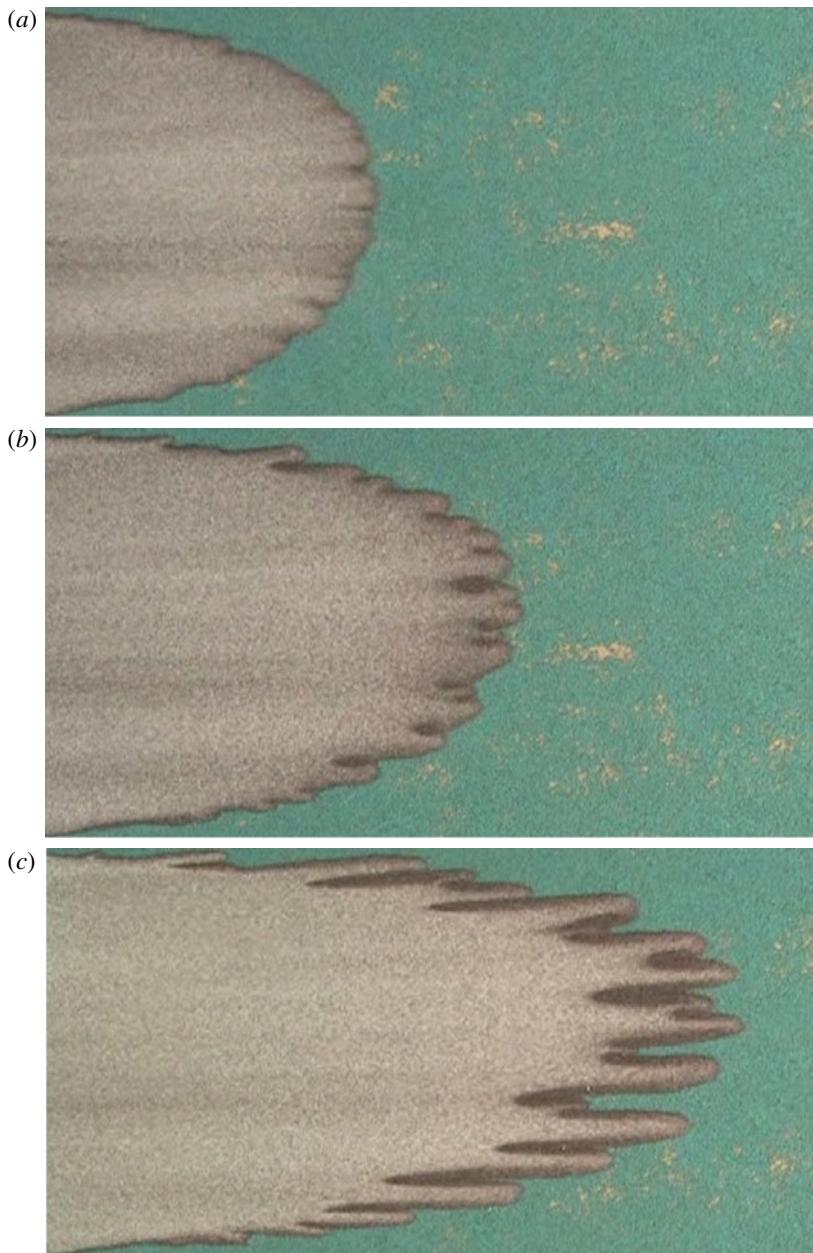
FIGURE 1. A sequence of overhead views of the laboratory experiment in which a bidisperse mixture of spherical (white) glass ballotini (75–150 μm) and irregular (brown) carborundum grains (315–350 μm) is released onto a plane inclined at $\zeta = 27°$. The chute surface is roughened with a monolayer of (turquoise) glass ballotini (750–1000 μm). Particle-size segregation and velocity shear through the avalanche preferentially transports large grains towards the flow front, where they may be overrun, but rise to the surface again by size segregation. The accumulation of the larger more resistive grains at the flow front (*a*) leads to a lateral instability (*b*) and the front degenerates into a series of distinct fingers (*c*). The images are approximately 57 cm × 30 cm. A movie showing the time-dependent evolution of this flow is available at http://dx.doi.org/10.1017/jfm.2012.348.

Observations of fingering instabilities in dense flows of bidisperse granular mixtures on inclined chutes demonstrate the crucial role of particle-size segregation (Pouliquen *et al.* 1997; Pouliquen & Vallance 1999; Félix & Thomas 2004; Goujon *et al.* 2007). Figures 1 and 2 show an example generated by the release of a finite mass of material from a reservoir onto an inclined plane. The bidisperse mixture is composed of (white) spherical glass ballotini (75–150 µm) and larger (brown) irregularly shaped carborundum particles (315–355 µm). When this bidisperse mixture flows down an inclined plane, roughened with (turquoise) glass ballotini (750–1000 µm), kinetic sieving and squeeze expulsion cause the large particles to segregate to the free surface. Velocity shear through the depth of the avalanche ensures that the large grains experience a greater velocity and they are preferentially transported towards the flow front. Here they may be overrun, but can rise to the surface again by size segregation and accumulate there (e.g. Pouliquen *et al.* 1997; Pouliquen & Vallance 1999; Gray & Ancey 2009) as can be seen in figure 1(*a,b*). If the large grains experience a greater frictional resistance to motion, which is achieved in experiments by using large irregular and small spherical grains, the front is observed to be unstable (Pouliquen *et al.* 1997; Pouliquen & Vallance 1999). Lateral variations in the proportion of large grains near the front cause inhomogeneities in the mobility of the boundary. In regions where there is a greater proportion of resistive large grains than the average, the mobility of the front is reduced and these large-rich regions lag behind the more mobile regions. Thus, a non-uniform front forms, composed of large-rich clefts of retarded mobility which trail behind and separate fingers of relatively more mobile material (Pouliquen & Vallance 1999). The front degenerates into a series of distinct fingers. Once the fingers have developed, additional large grains that reach the flow front are advected to the side to form static large-rich lateral levees, which confine the more mobile material within the channel.

The experimental observations are not precisely reproducible, with the position and length of the fingers varying within experimental runs in which the flow parameters are held constant, indicating a sensitivity of the evolution of the flow to small changes in the initial conditions (such as the initial particle-size distribution) and complicated interactions between the developing fingers. The accumulation of static regions of large material can cause deviation in the flow direction as shown in figure 2(*b*), and as the flow wanes, material can be seen draining off the raised lateral levees, exposing fines-rich material lining the interior of the channels as shown in figure 2(*c*). Fingering is an example of a 'segregation-mobility feedback effect' (Gray & Kokelaar 2010*a*,*b*) and the self-channelization of the flow that it causes has a significant effect on the run-out distance. This is therefore an essential consideration for hazard assessment in larger-scale geophysical mass flows, where the same process occurs (e.g Pierson 1986; Iverson & Vallance 2001; Johnson *et al.* 2012).

Motivated by the experimental observations of the segregation-induced break-up of the uniform flow front, Pouliquen & Vallance (1999) developed a phenomenological model of a bidisperse granular avalanche, which we discuss in detail in §2. The Pouliquen & Vallance (1999) model adopts depth-averaged equations to describe the conservation of mass and momentum in the avalanche, and considers the slow-flow limit where inertial contributions to the momentum balance are negligible. In addition, the distribution of large and small particles is assumed to be spatially and temporally invariant in a frame of reference moving with the steadily propagating front; the imposed concentration field is simply advected with the flow. The influence of the inhomogeneous particle size distribution on the flow is modelled by a concentration-dependent friction coefficient that enables the resistance experienced by the avalanche
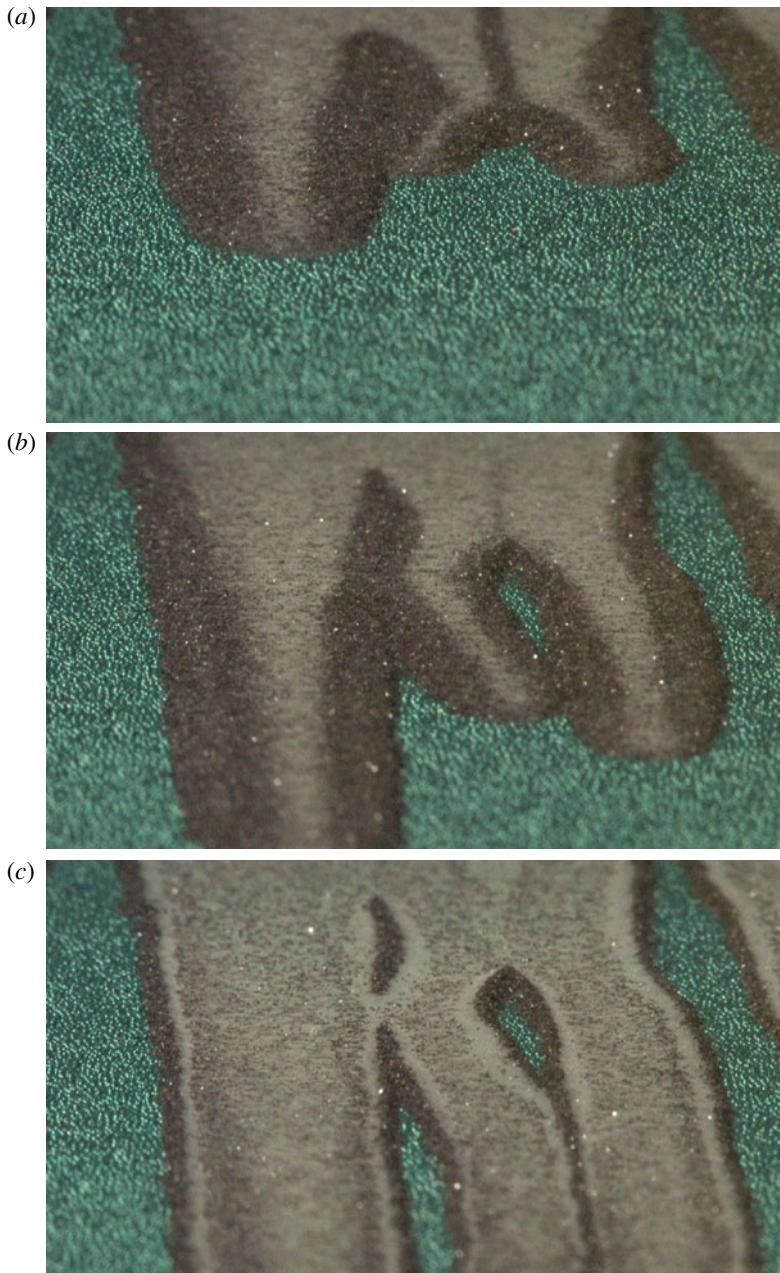
FIGURE 2. A sequence of oblique head-on views of the laboratory experiment shown in figure 1 in which a bidisperse mixture of spherical (white) ballotini and irregular (brown) carborundum grains moves down an inclined plane towards the camera. Large grains that are transported to the flow front are advected to the side to form lateral levees (*a*) that confine more mobile fines-rich material in a channel. The accumulation of static regions of large material can cause deviation in the flow direction (*b*), as seen here. In addition, as the flow wanes, material can be seen draining off the raised lateral levees, exposing fines-rich material lining the interior of the channels (*c*). A movie showing the time-dependent evolution of this flow is available at http://dx.doi.org/10.1017/jfm.2012.348.

to vary from a high value in regions where there is a high proportion of the frictional large particles to lower values in small-particle-rich regions. Pouliquen & Vallance (1999) performed a linear stability analysis of a propagating front and showed that monodisperse avalanches are linearly stable to small perturbations while bidisperse mixtures of resistive large particles and less frictional small particles are linearly unstable to transverse perturbations.

The simplifying assumptions adopted in the development of the Pouliquen & Vallance (1999) model render it inappropriate for a description of bidisperse granular avalanches from initiation to final deposition. In particular, the evolution of the particle-size distribution and the effect of segregation on the mobility of the avalanching material cannot be accounted for in their model. In this work we propose a simple model for fingering in dense, bidisperse granular avalanches that adopts a depth-averaged framework for both the conservation of mass and momentum within the avalanching layer (e.g. Gray, Tai & Noelle 2003), as well as for the evolving particle distribution (Gray & Kokelaar 2010*a*,*b*). This approach, which was suggested by Gray & Kokelaar (2010*a*,*b*), has the advantage that only two-dimensional fields need to be computed, whilst still being able to reproduce the bulk transport processes of the full three-dimensional equations. The segregation-mobility feedback can then be modelled through a concentration-dependent friction coefficient in the depth-averaged momentum balance, as in Pouliquen & Vallance (1999), although there are many other ways to couple the equations (see Gray & Kokelaar 2010*a*,*b*). This is not the only possible approach. For instance the bulk flow could also be coupled directly with the three-dimensional segregation equations by computing the bulk flow using the recent rheological models of Jop, Forterre & Pouliquen (2006) and Rognon *et al.* (2007), or alternatively by reconstructing the three-dimensional velocity field from the depth-averaged avalanche model by using assumed velocity profiles with depth. This latter approach was adopted by Gray & Ancey (2009) to construct exact solutions in a situation where there is no feedback between the particle segregation and bulk dynamics.

Depth-averaged (shallow-water) models have been shown to be an effective tool in modelling many geophysical mass flows, including snow avalanches (Cui, Gray & Jóhannesson 2007; Gruber & Bartelt 2007), dense pyroclastic flows (Mangeney *et al.* 2007; Doyle *et al.* 2008), debris flows (Iverson 1997; Denlinger & Iverson 2001), block and ash flows (Pitman *et al.* 2003; Dalbey *et al.* 2008) and lahars (Williams, Stinton & Sheridan 2008). In addition to these geological applications, depth-averaged models have been applied to describe small-scale laboratory experiments of dense granular flows containing obstacles (Gray *et al.* 2003), wedges (Gray *et al.* 2003; Hákonardóttir & Hogg 2005; Gray & Cui 2007) and contractions (Vreman *et al.* 2007), as well as flows on inclined planes that exhibit hydraulic jumps (Johnson & Gray 2011), which all show quantitative agreement between theory and experiment. The depth-averaged equations of mass and momentum conservation are obtained by integrating the three-dimensional governing equations through the avalanche depth. By exploiting the shallowness of the flow an asymptotic expansion of the depth-integrated equations can be performed, and the leading order balance is retained (see e.g. Savage & Hutter 1989; Gray, Wieland & Hutter 1999; Gray *et al.* 2003). In the resulting two-dimensional depth-averaged system of equations the gradients of the deviatoric stress tensor do not appear and the normal stress is hydrostatic, to leading order, so no constitutive theory is required.

This paper is organized as follows. In §2 we discuss the simple model of bidisperse granular avalanches proposed by Pouliquen & Vallance (1999). Our model represents a

significant extension of this model, in particular through a description of the evolution of the particle size distribution. In §3 we derive the depth-averaged segregation equation from a fully three-dimensional model of particle-size segregation (Gray & Thornton 2005). The depth-averaged equation we obtain describes the preferential transport of large particles towards the flow front and in §4 we couple this 'large-particle transport equation' to a depth-averaged model for dense granular avalanches. Numerical solutions of the depth-averaged model corresponding to a lock–release on an inclined chute are obtained in §5, where we demonstrate the coupled depth-averaged model is able to describe the accumulation of large particles at the flow front and the break up of the front into a series of fingers that look similar to those observed in experiments. However, we are unable to obtain a fully grid-resolved numerical solution and a linear stability analysis is performed in §6 to investigate the reasons for this.

2. Pouliquen and Vallance's model

Pouliquen & Vallance (1999) proposed a phenomenological model in an attempt to describe the mechanism initiating the instability of the propagating front of a bidisperse granular avalanche. The Pouliquen & Vallance (1999) model adopts a depth-averaged approach, exploiting the shallowness of the avalanching material in comparison to its extent, to propose a system of conservation equations for the evolution in time, t, and the spatial variation of the avalanche thickness, h, the depth-averaged velocity, $\overline{\boldsymbol{u}}$, and the depth-averaged concentration of small particles, $\overline{\phi}$, which can be written as

$$\frac{\partial h}{\partial t} + \frac{\partial}{\partial x}(h\overline{u}) + \frac{\partial}{\partial y}(h\overline{v}) = 0, \tag{2.1}$$

$$\tan \zeta - \mu \frac{\overline{u}}{|\overline{\boldsymbol{u}}|} - \frac{\partial h}{\partial x} = 0, \tag{2.2}$$

$$-\mu \frac{\overline{v}}{|\overline{\boldsymbol{u}}|} - \frac{\partial h}{\partial y} = 0, \tag{2.3}$$

$$\frac{\partial \overline{\phi}}{\partial t} + \overline{u}\frac{\partial \overline{\phi}}{\partial x} + \overline{v}\frac{\partial \overline{\phi}}{\partial y} = 0, \tag{2.4}$$

where ζ is the inclination of the slope with respect to the horizontal, μ is the basal friction coefficient, x and y are the downslope and cross-slope coordinates, respectively, and $\overline{\boldsymbol{u}} = (\overline{u}, \overline{v})$ denotes the depth-averaged velocity in the downslope and cross-slope directions (figure 3).

The depth-averaged mass balance equation (2.1) assumes that the densities of the large and small particles are equal and the avalanche is incompressible. While it is known that dilatation occurs when a granular packing is sheared (Reynolds 1885), the assumption of incompressibility during motion is frequently adopted for dense granular flows where observations show there is little change in volume during the motion (see e.g. Savage & Hutter 1989). In the depth-averaged momentum balance equations in the downslope and cross-slope directions, given by (2.2) and (2.3), respectively, the inertial terms are neglected in view of the low flow velocities observed in laboratory experiments. Furthermore, the earth pressure coefficient is assumed to remain constant at unity (see e.g. Savage & Hutter 1989; Gray *et al.* 2003). Pouliquen & Vallance (1999) do not describe fully the dynamics of particle-size
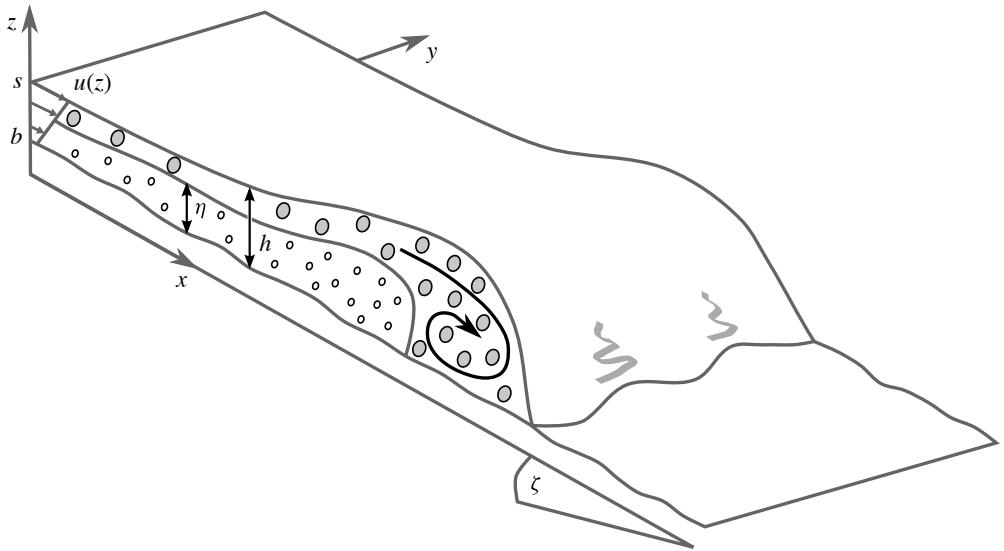
FIGURE 3. Sketch of a bidisperse granular avalanche. The granular material flows down a chute inclined at an angle ζ to the horizontal. A coordinate system is taken with the x-axis aligned with the downslope direction, the y-axis is aligned with the cross-slope direction and the z-axis is normal to the chute surface which has topography $z = b(x, y, t)$. The avalanching material has depth $h(x, y, t) = s(x, y, t) - b(x, y, t)$, where $z = s(x, y, t)$ denotes the surface of the avalanche, and propagates with a downslope velocity $u(x, y, z, t)$. We assume that particle-size segregation completely separates the particle classes, with large particles overlying small and separated by an interface at a height $\eta(x, y, t) = h\overline{\phi}$. The shear profile through the avalanche depth then preferentially transports the large particles to the flow front where they may be overrun, rise by segregation, recirculate and accumulate.

segregation, but simply enforce advection of an imposed particle distribution at the velocity of the bulk flow (2.4). The initial particle concentration profile is chosen to reflect the expected distribution of large and small particles and is then simply carried along with the avalanche, but does not evolve further during the flow. In particular, there is no additional accumulation of large material at the flow front. Note that, for consistency with the depth-averaged theory for particle-size segregation derived by Gray & Kokelaar (2010*a*,*b*), we have expressed the Pouliquen & Vallance (1999) model in terms of the depth-averaged concentration of small particles $\overline{\phi}$, rather than for the concentration of large particles (which here is given by $1 - \overline{\phi}$) as originally formulated by Pouliquen & Vallance (1999).

Currently, little is known about the frictional properties of bidisperse granular mixtures. Pouliquen & Vallance (1999) propose a bidisperse friction coefficient, which is a concentration-weighted average of the friction coefficients of the constituent particles in a pure phase. The most simple averaging assumes a linear weighting of the pure phase friction coefficients with the depth-averaged concentration,

$$\mu = (1 - \overline{\phi})\mu^L + \overline{\phi}\mu^S \tag{2.5}$$

where μ^L and μ^S denote the friction coefficients for pure phases of large and small particles, respectively. By adopting a friction coefficient of this form, the friction experienced by the bidisperse avalanche is coupled to the particle distribution. Pouliquen & Vallance (1999) propose that the friction coefficient of each phase can be

described by a rough bed friction law (Pouliquen 1999*a*) of the form

$$\mu^{\mathcal{N}}(h, |\overline{\boldsymbol{u}}|) = \tan \zeta_1^{\mathcal{N}} + (\tan \zeta_2^{\mathcal{N}} - \tan \zeta_1^{\mathcal{N}}) \exp\left(\frac{-\beta \sqrt{g} h^{3/2}}{\mathcal{L}^{\mathcal{N}} |\overline{\boldsymbol{u}}|}\right), \quad \mathcal{N} = L, S, \quad (2.6)$$

where $\beta = 0.136$ is an empirical constant and we use superscripts $\mathcal{N} = L, S$ to denote a quantity that is associated with large and small particles, respectively. The minimum angle for steady uniform flow, $\zeta_1^{\mathcal{N}}$, the maximum angle for steady uniform flow, $\zeta_2^{\mathcal{N}}$, and the length scale, $\mathcal{L}^{\mathcal{N}}$, are constants for a given granular material which can be determined experimentally (see e.g. Pouliquen 1999*a*). By adopting friction coefficients of the form (2.6) a total of six parameters are required to describe the material properties of the two constituent particle classes. Pouliquen & Vallance (1999) assume $\zeta_1^S < \zeta_1^L$ and $\zeta_2^S < \zeta_2^L$ so that the friction experienced by the large, irregular grains is larger than that experienced by the small, spherical grains. While the length scales $\mathcal{L}^S$ and $\mathcal{L}^L$ may differ for each particle class, we assume throughout that $\mathcal{L}^S = \mathcal{L}^L = \mathcal{L}$ for simplicity.

The simple advection equation for the concentration of small particles (2.4) is not sufficient to describe large-particle transport which leads to the formation and growth of a large-rich front. However, Pouliquen & Vallance (1999) consider a situation in which a large-rich flow front has already formed and enforce an initial condition with a depth-averaged concentration distribution of the form

$$\overline{\phi}(x, y, 0) = \frac{1}{2}\left(1 - \tanh\left(\frac{x + x_L}{D}\right)\right), \quad (2.7)$$

which is simply advected with the flow. Here x_L is the length of the large-rich front region and D is the length scale of the transition region between the large-rich front and the pure-fine region behind. Since the front is comprised entirely of large particles, the shape of the steadily propagating granular front can be determined from the balance of the gravitational force in the downslope direction which drives the motion with the frictional resistance opposing the motion (Pouliquen 1999*b*).

Pouliquen & Vallance (1999) investigate the linear stability of their model for monodisperse and bidisperse granular flows to small cross-slope perturbations. The linear stability analysis suggests that monodisperse fronts are stable, while bidisperse flows are unstable if $\mu^L > \mu^S$, i.e. if the large material at the flow front experiences greater frictional resistance than the small grains. Furthermore, the linear stability analysis found that, for linearly unstable flows, the growth rate is an increasing function of the (transverse) wavenumber. Therefore, the system of equations proposed by Pouliquen & Vallance (1999) is unable to predict the wavelength of the fingers.

3. The two-dimensional depth-averaged segregation equation

While the phenomenological model proposed by Pouliquen & Vallance (1999) provides a basis for modelling bidisperse granular avalanches it cannot fully describe the evolution of the avalanche from the initiation of the flow to the final deposition of the material. In particular, as the spatial distribution of the constituent particle classes is imposed as an initial condition and simply advected with the bulk flow, the segregation-mobility feedback between the evolving particle-size distribution and the bulk flow cannot be fully described.

Models of particle-size segregation in granular mixtures within a shearing flow have been derived using information entropy theory (Savage & Lun 1988), *ad-hoc*

methods (Dolgunin & Ukolov 1995) and mixtures theory (Gray & Thornton 2005; Thornton *et al.* 2006; Gray & Chugunov 2006; Gray & Ancey 2011). The resulting 'segregation equations' have been shown to be capable of reproducing several features of the flow of bidisperse granular mixtures (Gray & Ancey 2009; May *et al.* 2010; Wiederseiner *et al.* 2011). However, to use the three-dimensional segregation equation to describe particle transport within the avalanche we require knowledge of the velocity profile in the interior of the avalanche. Therefore, it is not possible to utilize the three-dimensional segregation equation in conjunction with the commonly used depth-averaged models of avalanche motion (e.g. Savage & Hutter 1989; Gray *et al.* 1999) unless we make additional assumptions on the form of the velocity profile within the avalanche.

Recently, the two-dimensional segregation equation has been depth-averaged (Gray & Kokelaar 2010*a,b*), allowing a description of particle-size segregation to be placed alongside depth-averaged models of granular avalanches. The depth-averaged segregation equation provides a simplified description of the complicated evolving particle-size distributions, which are obtained as solutions of the two- and three-dimensional segregation equation (Gray & Kokelaar 2010*a,b*). Furthermore, by coupling the particle concentration, whose evolution is described by the depth-averaged segregation equation, to the depth-averaged equations of mass and momentum conservation (Savage & Hutter 1989; Gray *et al.* 1999), models of the segregation-mobility feedback can be formed (Gray & Kokelaar 2010*a,b*).

In order to model the fingering instabilities in bidisperse granular avalanches we generalize the depth-averaged segregation theory of Gray & Kokelaar (2010*a,b*) which is derived for two-dimensional flows, to fully three-dimensional flows. The most general form of the dimensionless segregation equation (e.g. Dolgunin & Ukolov 1995; Gray & Chugunov 2006) for the volume fraction of small particles ϕ is

$$\frac{\partial \phi}{\partial t} + \frac{\partial}{\partial x}(\phi u) + \frac{\partial}{\partial y}(\phi v) + \frac{\partial}{\partial z}(\phi w) - \frac{\partial}{\partial z}(S_r \phi(1-\phi)) = \frac{\partial}{\partial z}\left(D_r \frac{\partial \phi}{\partial z}\right), \quad (3.1)$$

where x and y are coordinates in the downslope and cross-slope directions, respectively, and z is normal to the chute. The bulk velocity $\boldsymbol{u}$ has components (u, v, w) in the downslope, cross-slope and normal directions, respectively, and the dimensionless parameters S_r and D_r are the (dimensionless) segregation rate and diffusivity, respectively (Gray & Thornton 2005; Gray & Chugunov 2006). The volume fraction of large particles is given by $1 - \phi$. At the free surface, $z = s(x, y, t)$, and base, $z = b(x, y, t)$, we enforce kinematic boundary conditions (e.g. Savage & Hutter 1989; Gray *et al.* 1999) of the form

$$\frac{\partial s}{\partial t} + u_s \frac{\partial s}{\partial x} + v_s \frac{\partial s}{\partial y} - w_s = 0 \quad \text{on } z = s(x, y, t), \quad (3.2)$$

$$\frac{\partial b}{\partial t} + u_b \frac{\partial b}{\partial x} + v_b \frac{\partial b}{\partial y} - w_b = 0 \quad \text{on } z = b(x, y, t), \quad (3.3)$$

where the subscripts s and b on the velocity components denote evaluation at the surface and base of the flow, respectively. In addition, there is no flux of either the large or small particles across the upper free surface or the lower base of the flow,

$$S_r \phi(1-\phi) + D_r \frac{\partial \phi}{\partial z} = 0 \quad \text{at } z = s, b. \quad (3.4)$$

The segregation equation (3.1) can be integrated through the avalanche depth by using Leibniz' integral theorem (Abramowitz & Stegun 1970) to give

$$\frac{\partial}{\partial t}(h\overline{\phi}) + \frac{\partial}{\partial x}(h\overline{\phi u}) + \frac{\partial}{\partial y}(h\overline{\phi v}) = \left[\phi\left(\frac{\partial z}{\partial t} + u\frac{\partial z}{\partial x} + v\frac{\partial z}{\partial y} - w\right)\right]_b^s$$
$$+ \left[S_r\phi(1-\phi) + D_r\frac{\partial\phi}{\partial z}\right]_b^s, \quad (3.5)$$

where the depth-averaged small-particle concentration $\overline{\phi}$ and the depth-averaged small-particle fluxes in the downslope and cross-slope directions, $\overline{\phi u}$ and $\overline{\phi v}$, respectively, are defined as

$$\overline{\phi} = \frac{1}{h}\int_b^s \phi\,dz, \quad \overline{\phi u} = \frac{1}{h}\int_b^s \phi u\,dz, \quad \overline{\phi v} = \frac{1}{h}\int_b^s \phi v\,dz, \quad (3.6)$$

and $h(x, y, z, t) = s - b$. On application of the kinematic boundary conditions (3.2) and (3.3) and the no-flux conditions (3.4) at the free surface and at the base of the avalanche, the depth-averaged segregation equation (3.5) reduces to

$$\frac{\partial}{\partial t}(h\overline{\phi}) + \frac{\partial}{\partial x}(h\overline{\phi u}) + \frac{\partial}{\partial y}(h\overline{\phi v}) = 0. \quad (3.7)$$

In order to close the model expressions are required to relate the depth-averaged concentration fluxes to the depth-averaged flow velocity. While it is possible to construct a hierarchy of models by assuming a variety of concentration and velocity profiles through the avalanche depth, here we propose simple physically motivated profiles of the concentration and avalanche velocity, following Gray & Kokelaar (2010a,b). The two constituents are assumed to segregate rapidly in the avalanche into fully separated inversely graded layers, as has been observed in stratification pattern experiments (Gray & Hutter 1997; Gray & Ancey 2009). The concentration of small particles within the avalanching layer is then taken to be

$$\phi(x, y, z, t) = \begin{cases} 0, & l < z < s, \\ 1, & b < z < l, \end{cases} \quad (3.8)$$

where $z = l(x, y, t)$ is the height of the interface between the small-particle phase and the overlying large-particle phase. Furthermore, following Gray & Kokelaar (2010a,b), we assume that the velocity profile within the avalanching layer is linear with depth, with the greatest velocities achieved at the surface of the flow. We therefore take velocity profiles of the form

$$\left.\begin{aligned} u &= \alpha\overline{u} + 2(1-\alpha)\overline{u}\left(\frac{z-b}{h}\right), \\ v &= \alpha\overline{v} + 2(1-\alpha)\overline{v}\left(\frac{z-b}{h}\right). \end{aligned}\right\} \quad (3.9)$$

These profiles ensure the depth-averaged downslope and cross-slope velocities are $\overline{u}$ and $\overline{v}$, respectively. The parameter $\alpha \in [0, 1]$ allows the velocity profile to vary from plug flow (for $\alpha = 1$) to simple shear with no slip at the base ($\alpha = 0$). For $0 < \alpha < 1$ the velocity profiles are linear through the depth of the avalanche with a non-zero slip velocity at the basal boundary. While more complicated, nonlinear velocity profiles can be incorporated, the linear profiles capture the essential features of shear through the avalanching layer and the possibility of basal slip.

Evaluating the integrals (3.6) with the inversely graded concentration profile (3.8) and velocity profile (3.9) the depth-averaged concentration and depth-averaged concentration fluxes are

$$\left.\begin{array}{l} h\overline{\phi} = \eta, \\ h\overline{\phi u} = h\overline{u}\,\overline{\phi} - (1-\alpha)h\overline{u}\,\overline{\phi}(1-\overline{\phi}), \\ h\overline{\phi v} = h\overline{v}\,\overline{\phi} - (1-\alpha)h\overline{v}\,\overline{\phi}(1-\overline{\phi}), \end{array}\right\} \quad (3.10)$$

where $\eta(x, y, t) = l - b$ is the thickness of the small-particle layer. With these expressions for the depth-averaged concentration and depth-averaged concentration fluxes, the depth-averaged segregation equation (3.7) can be written as

$$\frac{\partial \eta}{\partial t} + \frac{\partial}{\partial x}\left(\eta\overline{u} - (1-\alpha)\eta\overline{u}\left(1 - \frac{\eta}{h}\right)\right) + \frac{\partial}{\partial y}\left(\eta\overline{v} - (1-\alpha)\eta\overline{v}\left(1 - \frac{\eta}{h}\right)\right) = 0, \quad (3.11)$$

which is the two-dimensional equivalent of the depth-averaged segregation equation derived by Gray & Kokelaar (2010a,b). They refer to (3.11) as the 'large-particle transport equation' because it describes the preferential transport of large particles, which lie in the higher, faster-moving regions of the flow, towards the flow front.

Gray & Kokelaar (2010a,b) examined the properties of (3.11) for unidirectional downslope flows, using a prescribed velocity field and avalanche thickness. The depth-averaged theory provides a simple representation of the complicated evolution of the particle size distribution, yet it is capable of reproducing many features of unidirectional flow solutions to the hyperbolic segregation equation (3.1) with $D_r \equiv 0$ and no variation in the cross-slope (y) direction (Gray, Shearer & Thornton 2006; Shearer, Gray & Thornton 2008). In particular, once inversely graded fully segregated layers have developed, the motion of the interface as determined by solution of the two-dimensional hyperbolic theory is reproduced precisely by the one-dimensional depth-averaged equation, provided that the interface does not break (Gray & Kokelaar 2010a,b). When the interface does break, the breaking size-segregation wave predicted in the two-dimensional hyperbolic theory (Thornton & Gray 2008; McIntyre *et al.* 2008; Gray & Ancey 2009) is represented by a concentration shock in the depth-averaged theory (Gray & Kokelaar 2010a,b). The speed of the shock is identical to the propagation speed of the breaking size-segregation wave and the net transport of large particles remains identical to that which occurs in the hyperbolic segregation model. The recirculation of large particles that are overridden by the advancing flow front and are lifted back towards the free surface by particle-size segregation is a crucial process in the development of leveed fingers (Pouliquen & Vallance 1999). In the non-depth-averaged models this is represented as a breaking size-segregation wave (Thornton & Gray 2008; McIntyre *et al.* 2008; Gray & Ancey 2009; Johnson *et al.* 2012), that picks up slowly moving large grains near the base of the flow and transports them to higher faster-moving near-surface regions, to create a recirculation loop. In the depth-averaged formulation (Gray & Kokelaar 2010a,b) the breaking wave is replaced by a shock, which instantaneously lifts large particles to the high faster-moving surface layers (Gray & Kokelaar 2010a,b). The depth-averaged equation (3.11) is therefore capable of describing the net transport of large particles towards an avalanche front and their subsequent accumulation there.

4. A fully coupled theory for segregation-mobility feedback

We model the segregation-mobility feedback in bidisperse granular avalanches through a coupling of the large-particle transport equation (3.11) to a depth-averaged model for the bulk flow (e.g. Gray *et al.* 2003).

4.1. *Governing equations*

Dimensionless variables are introduced through application of standard scalings appropriate for depth-averaged equations describing dense granular flows (Savage & Hutter 1989; Gray *et al.* 1999),

$$(h', \eta') = H(h, \eta), \quad (x', y') = L(x, y), \quad (\overline{u}', \overline{v}') = \sqrt{gL}(\overline{u}, \overline{v}), \quad t' = \sqrt{L/g}t, \quad (4.1)$$

where the primed variables are dimensional and g denotes the constant of gravitational acceleration. With these scalings the dimensionless system of governing equations describing the evolution of the avalanche thickness, h, the depth-averaged bulk velocity, $\overline{\boldsymbol{u}} = (\overline{u}, \overline{v})$, and the height of the interface between small particles and overlying large particles, $\eta = h\overline{\phi}$, consists of four depth-averaged conservation equations,

$$\frac{\partial h}{\partial t} + \frac{\partial}{\partial x}(h\overline{u}) + \frac{\partial}{\partial y}(h\overline{v}) = 0, \quad (4.2)$$

$$\frac{\partial}{\partial t}(h\overline{u}) + \frac{\partial}{\partial x}(h\overline{u}^2) + \frac{\partial}{\partial y}(h\overline{u}\,\overline{v}) + \frac{\partial}{\partial x}\left(\frac{1}{2}\epsilon h^2 \cos\zeta\right) = hS_{(x)}, \quad (4.3)$$

$$\frac{\partial}{\partial t}(h\overline{v}) + \frac{\partial}{\partial x}(h\overline{u}\,\overline{v}) + \frac{\partial}{\partial y}(h\overline{v}^2) + \frac{\partial}{\partial y}\left(\frac{1}{2}\epsilon h^2 \cos\zeta\right) = hS_{(y)}, \quad (4.4)$$

$$\frac{\partial \eta}{\partial t} + \frac{\partial}{\partial x}\left(\eta\overline{u} - (1-\alpha)\eta\overline{u}\left(1 - \frac{\eta}{h}\right)\right) + \frac{\partial}{\partial y}\left(\eta\overline{v} - (1-\alpha)\eta\overline{v}\left(1 - \frac{\eta}{h}\right)\right) = 0, \quad (4.5)$$

where the source terms $S_{(x)}$ and $S_{(y)}$ consist of the components of gravitational acceleration, basal friction and local basal topography,

$$S_{(x)} = \sin\zeta - \mu\frac{\overline{u}}{|\overline{\boldsymbol{u}}|}\cos\zeta - \epsilon\frac{\partial b}{\partial x}\cos\zeta, \quad (4.6)$$

$$S_{(y)} = -\mu\frac{\overline{v}}{|\overline{\boldsymbol{u}}|}\cos\zeta - \epsilon\frac{\partial b}{\partial y}\cos\zeta. \quad (4.7)$$

The basal friction is of Coulomb type, with the frictional shear stress proportional to the normal stress (the coefficient of proportionality being the friction coefficient μ), and opposes the direction of motion. Throughout our analysis we will consider flows on planar inclines, thus we take $b(x, y, t) \equiv 0$. The dimensionless aspect ratio $\epsilon = H/L$ is the ratio of a typical avalanche thickness H to a typical length L. In the derivation of the equations for the conservation of mass and momentum (4.2)–(4.4) it is assumed that the densities of each of the particle classes are identical, and the mixture is incompressible and has a lithostatic pressure through its depth (Savage & Hutter 1989; Gray *et al.* 1999), which are consistent with the assumptions on which the large-particle transport equation (4.5) has been derived (Gray & Kokelaar 2010*a*,*b*). While the bulk flow equations (4.2)–(4.4) are relatively simple, they have been applied successfully to model complex granular flows in which both normal and oblique shock waves develop as a monodisperse avalanche flows past an obstacle or through a constriction (Gray *et al.* 2003; Hákonardóttir & Hogg 2005; Gray & Cui 2007;

Vreman *et al.* 2007; Cui *et al.* 2007) as well as the flow after the impingement of a jet on an inclined plane (Johnson & Gray 2011). In the equations for the conservation of momentum (4.3) and (4.4) it has been implicitly assumed that $\overline{u^2} \equiv \bar{u}^2$, which is only strictly true in the case where u is independent of z. This assumption can be relaxed by the introduction of 'shape factors' (see e.g Savage & Hutter 1989), but for most observed vertical velocity profiles (see e.g. GDR MiDi 2004) these shape factors are close to unity, so for simplicity will not be included here. In addition, earth pressure coefficients (e.g. Savage & Hutter 1989; Gray *et al.* 1999; Iverson & Denlinger 2001), which model differences in the normal stress components, can be included, but are neglected here.

The system of conservation laws (4.2)–(4.5) are closely related to the system (2.1)–(2.4) proposed by Pouliquen & Vallance (1999). In particular, the equation of mass conservation is identical, while the momentum balance equations (2.2) and (2.3) are obtained from (4.3) and (4.4), respectively, by neglecting the inertial terms in comparison to the pressure gradient and source terms, and taking a planar basal topography $b(x, y, t) = 0$. The large-particle transport equation (4.5) also reduces to the advection equation (2.4) when there is no shear ($\alpha = 1$, indicating no preferential transport of large particles), or when there is a pure phase of either all large or all small particles. The system studied by Pouliquen & Vallance (1999) therefore represents a particular limit of the depth-averaged system (4.2)–(4.5) in which the avalanche propagation is sufficiently slow that inertial terms can be neglected and there is no preferential transport of large particles towards the front of the avalanche. This corresponds to the situation in which all of the large particles have already accumulated in a pure phase at the flow front. The depth-averaged system of equations we propose (4.2)–(4.5) allows a description of the evolution of the particle size distribution from a bidisperse, inversely graded avalanche to an avalanche with a large-rich front, and we can assess the effects of this evolving size distribution on the mobility of the avalanche.

4.2. *Friction model for a bidisperse mixture*

The Pouliquen (1999*a*) friction coefficient $\mu^{\mathcal{N}}$ for constituent $\mathcal{N} = L, S$, defined in (2.6), is a function of the avalanche depth, h, and the depth-averaged velocity, $\bar{u}$. The use of the depth-averaged velocity rather than the basal avalanche velocity implies that it parameterizes, or approximates, some aspects of the rheology within the granular layer, as well as the friction experienced at the base (Forterre & Pouliquen 2008). This suggests that the effective bed friction for a dense bidisperse granular flow, which has segregated into layers composed of distinct grain classes, does not simply depend on the properties of the grains in contact with the bed. Rather the friction law should encompass properties of the overlying grains. This was recognized by Pouliquen & Vallance (1999) in their study of bidisperse granular avalanches. In the absence of a composite rheology or an empirical bed friction for a bidisperse mixture, Pouliquen & Vallance (1999) proposed a simple effective bed friction, which is a concentration-weighted average of the friction coefficients of each particle class, given by (2.5). This can be recast in terms of the height of the interface, η, and the depth of the avalanche, h, as

$$\mu = \left(1 - \frac{\eta}{h}\right) \mu^L + \frac{\eta}{h} \mu^S. \tag{4.8}$$

Such concentration-dependent friction in the source terms represents a relatively weak coupling of the model, since the derivative terms in the system of equations (4.2)–(4.5)

are not affected. It nevertheless provides a simple way of increasing the frictional resistance to motion as the proportion of irregular large particles increases. Alternative forms of the friction law are possible. For instance, the basal friction might also reasonably be parameterized by switching between the large and small particle laws by a weighting based on the concentration of particles at the base of the avalanche, rather than the depth-averaged concentration. For the sharp particle size distribution assumed in (3.8) this would imply the friction at the bed would be the small-particle friction, unless there were no small particles, and it would discontinuously jump to large-particle friction. We have implemented this version of the friction law in numerical computations, with a rapid variation between the friction coefficients of the grain classes adopted for numerical convenience, but it has little qualitative effect on the fingering instability that develops. This is perhaps not surprising, since the friction law (4.8) provides for a discontinuous change in the friction coefficient between the pure phases and mixed regions, and between neighbouring regions of purely large and purely small grains, as the concentration changes discontinuously in the hyperbolic theory at shocks in the interface height.

Following Pouliquen & Vallance (1999) we model the frictional interaction of each of the constituent particle classes with the basal surface using an empirical friction law for dense granular flows on a rough bed (Pouliquen 1999a), as given in dimensional variables in (2.6). On application of the scalings (4.1), the friction coefficient of a single particle species can be written as

$$\mu^{\mathcal{N}}(h, |\overline{\boldsymbol{u}}|) = \tan \zeta_1^{\mathcal{N}} + \left(\tan \zeta_2^{\mathcal{N}} - \tan \zeta_1^{\mathcal{N}}\right) \exp\left(\frac{-\beta \sqrt{\epsilon} h^{3/2}}{\mathcal{L}^{\mathcal{N}} |\overline{\boldsymbol{u}}|}\right), \quad \mathcal{N} = L, S, \text{ (4.9)}$$

where the length scale over which the friction coefficient varies has been scaled on the avalanche depth (i.e. the dimensional length scale $\mathcal{L}' = H\mathcal{L}$). The frictional length scale is a material property of the grains and bed, and typically $\mathcal{L} \in [0.05, 2]$ (Pouliquen 1999a). We recall $\beta = 0.136$ is an empirical dimensionless constant. The bidisperse friction coefficient, obtained by combining (4.8) and (4.9), is a function of the local avalanche depth, flow speed and concentration of small particles $\overline{\phi} = \eta/h$.

The empirical friction model (4.9) introduces five dimensionless material parameters that describe the frictional properties of the mixture. The friction angles ζ_1^L, ζ_1^S must be exceeded in order to maintain a steady flow of pure phases of large and small particles, respectively, the friction angles ζ_2^L, ζ_2^S are the maximum angles for which a steady flow of each constituent exists and the length scale $\mathcal{L}$ characterizes the variation of the friction coefficient, which we have assumed is identical for each of the particle classes. In addition to these five material parameters, a further three dimensionless controlling parameters can be identified in the governing equations (4.2)–(4.5) which we recognize as the inclination angle of the slope, ζ, the typical aspect ratio of the avalanche, $\epsilon = H/L \ll 1$, and the parameter $\alpha \in [0, 1]$ that determines the linear shear profile through the avalanche depth and the extent of basal slip. Furthermore, on specifying a velocity boundary condition, a dimensionless Froude number can be constructed, as discussed below.

The system of equations (4.2)–(4.9) reduces to the system of equations for a monodisperse granular avalanche when $\eta \equiv 0$ (representing an avalanche composed entirely of the large-particle class) and when $\eta \equiv h$ (for an avalanche of the small-particle class).

4.3. *Steady, fully developed flow*

A simple solution of the governing equations, corresponding to a steady, fully developed flowing layer can be determined by seeking a solution in which all fields are spatially and temporally invariant. In view of the scalings (4.1) the steady, fully developed solution can be written as

$$h(x, y, t) = h_0 = 1, \quad \bar{u}(x, y, t) = \bar{u}_0, \quad \bar{v}(x, y, t) = 0, \quad \eta(x, y, t) = \eta_0, \quad (4.10)$$

where $\bar{u}_0 > 0$ and $\eta_0 \in [0, 1]$ are constants to be determined.

On substitution into the downslope component of the momentum conservation equation (4.3) we find that the basal friction on the avalanche must balance the gravitational acceleration in order for a steady flow to be maintained,

$$\mu(1, \bar{u}_0, \eta_0) = \tan \zeta. \quad (4.11)$$

This can be written as

$$\mu_0^L + (\mu_0^S - \mu_0^L)\eta_0 = \tan \zeta, \quad (4.12)$$

where

$$\mu_0^{\mathcal{N}} = \mu^{\mathcal{N}}(1, \bar{u}_0) = \tan \zeta_1^{\mathcal{N}} + \left(\tan \zeta_2^{\mathcal{N}} - \tan \zeta_1^{\mathcal{N}}\right) \exp\left(\frac{-\beta\sqrt{\epsilon}}{\mathcal{L}\bar{u}_0}\right) \quad \text{for } \mathcal{N} = L, S. \quad (4.13)$$

For a prescribed concentration of large particles, which in the depth-averaged theory corresponds to a specified interface height η_0, the depth-averaged velocity of the avalanching layer is then given by

$$\bar{u}_0 = -\gamma / \log \chi, \quad (4.14)$$

where $\gamma = \beta\sqrt{\epsilon}/\mathcal{L}$ and

$$\chi = \frac{\tan \zeta - (1 - \eta_0)\tan \zeta_1^L - \eta_0 \tan \zeta_1^S}{(1 - \eta_0)(\tan \zeta_2^L - \tan \zeta_1^L) + \eta_0(\tan \zeta_2^S - \tan \zeta_1^S)}. \quad (4.15)$$

In order to obtain a physically appropriate avalanche velocity we must have $0 < \chi < 1$, from which we determine the range of inclinations angles for which the steady flow is possible,

$$(1 - \eta_0) \tan \zeta_1^L + \eta_0 \tan \zeta_1^S < \tan \zeta < (1 - \eta_0) \tan \zeta_2^L + \eta_0 \tan \zeta_2^S. \quad (4.16)$$

4.4. *Characteristic wave speeds*

The coupling of the transport equation (4.5) to the equations for conservation of mass and momentum (4.2)–(4.4) through the source terms and the empirical relations for the friction coefficients (4.9) do not involve gradients of the field variables. Therefore, the system of equations (4.2)–(4.5) is a quasi-linear, non-strictly hyperbolic system and characteristic surfaces along which information is propagated can be constructed.

Following Courant & Hilbert (1962) we find three characteristic surfaces. Two of these are rays (i.e. lines in the three-dimensional *xyt* space) defined by

$$Q_0: \quad dx = \bar{u}\, dt, \quad dy = \bar{v}\, dt, \quad (4.17)$$

$$Q_1: \quad dx = (1 - (1 - \alpha)(1 - 2\eta/h))\bar{u}\, dt, \quad dy = (1 - (1 - \alpha)(1 - 2\eta/h))\bar{v}\, dt. \quad (4.18)$$

The ray Q_0 propagates information with the bulk flow, while Q_1 propagates information at the velocity of the interface between the large and small grains.

We note the characteristics Q_0 and Q_1 coincide for $\alpha \equiv 1$ or when $\eta/h = 1/2$. The third characteristic surface is the usual characteristic conoid which is obtained for the shallow-water equations (Courant & Hilbert 1962; Weiyan 1992) and is defined by the Monge equation (Courant & Hilbert 1962)

$$Q_s: \quad (\mathrm{d}x - \bar{u}\,\mathrm{d}t)^2 + (\mathrm{d}y - \bar{v}\,\mathrm{d}t)^2 = h\epsilon \cos\zeta\,(\mathrm{d}t)^2, \tag{4.19}$$

which corresponds to the propagation of surface gravity waves, whose speed is given by $c_s = \sqrt{h\epsilon \cos\zeta}$ and which spread isotropically in a frame of reference moving with the bulk flow velocity. As the characteristic conoid Q_s is identical to the characteristic conoid of the shallow-water equations we can define a Froude number

$$Fr = \frac{|\bar{\boldsymbol{u}}|}{\sqrt{h\epsilon \cos\zeta}}, \tag{4.20}$$

as the ratio of the speed of the bulk flow to the speed of surface gravity waves. The flow is subcritical if $Fr < 1$ since the line $x = y = 0$ remains within the characteristic conoid for all $t > 0$, and is supercritical if $Fr > 1$ since the ray conoid does not intersect the t-axis for $t > 0$. Note that the Froude number is spatially and temporally varying, so the flow can transition between subcritical and supercritical states during the evolution of the flow.

While the characteristic ray Q_0 remains within the characteristic conoid Q_s, the ray Q_1 can be within the conoid, intersect the conoid or be outside of the conoid. These possibilities can be observed by considering the characteristic surfaces corresponding to the steady, fully developed flow described above. The characteristic surfaces for the steady, fully developed flow given by $h = 1$, $\bar{u} = \bar{u}_0$, $\bar{v} = 0$, $\eta = \eta_0$ are

$$\left.\begin{aligned}
Q_0: \quad & \mathrm{d}x = \bar{u}_0\,\mathrm{d}t, \quad \mathrm{d}y = 0, \\
Q_1: \quad & \mathrm{d}x = (1 - (1 - \alpha)(1 - 2\eta_0))\bar{u}_0\,\mathrm{d}t, \quad \mathrm{d}y = 0, \\
Q_s: \quad & (\mathrm{d}x - \bar{u}_0\,\mathrm{d}t)^2 + (\mathrm{d}y)^2 = \epsilon \cos\zeta\,(\mathrm{d}t)^2.
\end{aligned}\right\} \tag{4.21}$$

We take parameters $\zeta = 31°$, $\zeta_1^L = 27°$, $\zeta_2^L = 37°$, $\zeta_1^S = 20°$, $\zeta_2^S = 30°$ (corresponding to a mixture for which the large material experiences greater frictional resistance than the small material), $\mathscr{L} = 0.5$ and take $\epsilon = 0.1$. By varying the proportion of large material, through the choice of the steady interface height η_0, we obtain different steady flow velocities and the topology of the characteristic surfaces changes, as shown in figure 4, where local characteristic ray surfaces (i.e. the curves $Q_i|_{t=1}$ corresponding to the intersection of the characteristic surfaces and the plane $t = 1$) in the xy-plane are shown for various cases. The topology of the characteristic surfaces is determined by the speed of information propagation on the interface between the large and small particles in comparison to the speed of surface gravity waves. A critical velocity, $\bar{u}_c$, can be identified as the velocity at which the characteristic ray Q_1 coincides with the ray cone Q_s and is given by

$$\bar{u}_c = \frac{\sqrt{\epsilon \cos\zeta}}{|(1 - \alpha)(1 - 2\eta_0)|}. \tag{4.22}$$

For steady flow velocities $0 < \bar{u}_0 < \bar{u}_c$ the characteristic ray Q_1 remains within the characteristic ray cone Q_s. In contrast, if $\bar{u}_0 > \bar{u}_c > 0$ the characteristic ray Q_1 lies outside the ray cone Q_s. Note that

$$\frac{\bar{u}_0}{\bar{u}_c} = |(1 - \alpha)(1 - 2\eta_0)|\frac{\bar{u}_0}{\sqrt{\epsilon \cos\zeta}} \leqslant Fr, \tag{4.23}$$
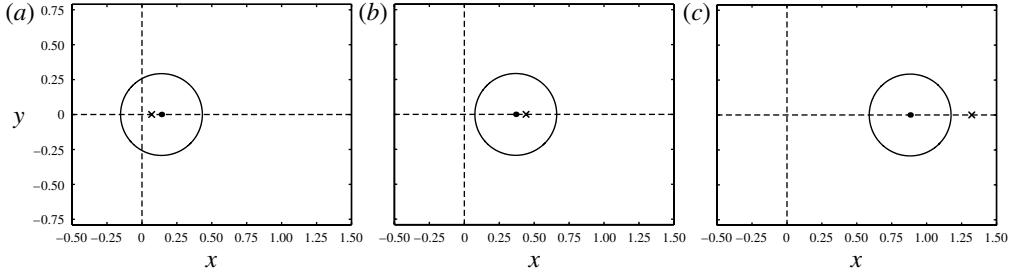
FIGURE 4. Characteristic ray surfaces, Q_s (solid line), Q_0 (·) and Q_1 (×), on the xy-plane at $t = 1$ for steady, fully developed flows on a plane inclined at an angle $\zeta = 31°$, for material with friction parameters $\zeta_1^L = 27°$, $\zeta_2^L = 37°$, $\zeta_1^S = 20°$, $\zeta_2^S = 30°$, $\mathcal{L} = 0.5$, and with $\epsilon = 0.1$ and $\alpha = 0$: (a) $\eta_0 = 0.25$, $\bar{u}_0 = 0.140$ and $\bar{u}_c = 0.590$ resulting in a subcritical flow with the characteristic rays lying within the ray cone; (b) $\eta_0 = 0.6$, $\bar{u}_0 = 0.370$ and $\bar{u}_c = 1.46$ resulting in a supercritical flow with the characteristic rays lying within the ray cone; (c) $\eta_0 = 0.75$, $\bar{u}_0 = 0.882$ and $\bar{u}_c = 0.590$ resulting in a supercritical flow with the characteristic ray corresponding to the speed of the interface lying outside the ray cone.

(with equality for $\eta_0 = 0$ and $\eta_0 = 1$ with $\alpha = 0$, i.e. for monodisperse flows with a simple shear velocity profile) so the ray Q_1 can only lie outside of the ray cone Q_s when the flow is supercritical ($Fr > 1$).

5. Two-dimensional numerical solutions for a propagating front

To test whether the system of equations (4.2)–(4.9) is able to generate fingers we perform numerical computations to simulate the laboratory experiments of Pouliquen & Vallance (1999). As the quasi-linear system of equations (4.2)–(4.5) is (non-strictly) hyperbolic we employ the non-oscillatory central scheme of Jiang & Tadmor (1998). This is a high-resolution shock-capturing scheme, which has been employed extensively to compute numerical solutions of shallow granular flows. For example, Gray *et al.* (2003) use this scheme to compute the dry granular free-surface flow past a pyramid and Gray & Cui (2007) adapted the scheme, employing body-fitted coordinates, to study granular avalanches impinging on an oblique wedge.

We calculate two-dimensional solutions of the depth-averaged systems of equations representing the flow of material out of a hopper with a fixed height onto an inclined plane. A computational domain $0 \leqslant x \leqslant L_x$ and $0 \leqslant y \leqslant L_y$ is employed, with periodic boundary conditions at $y = 0$ and $y = L_y$. For initial conditions we impose

$$h(x, y, 0) = 0, \quad \bar{u}(x, y, 0) = 0, \quad \bar{v}(x, y, 0) = 0, \quad \eta(x, y, 0) = 0, \tag{5.1}$$

representing a chute that is free of material. At $x = 0$, inflow conditions are prescribed with

$$\left.\begin{array}{ll} h(0, y, t) = 1 - e^{-t/\lambda}, & \bar{u}(0, y, t) = \bar{u}_0, \\ \bar{v}(0, y, t) = 0, & \eta(0, y, t) = \eta_0 + \eta_p(y), \end{array}\right\} \tag{5.2}$$

where $\bar{u}_0$ and η_0 are the depth-averaged flow velocity and interface height, respectively, for a steady, fully developed flow which are related by (4.14). Note, for numerical convenience we allow the flow depth to gradually attain the steady value $h = 1$, and introduce a time scale λ to characterize this evolution. The long time evolution of the numerical solutions we obtain are insensitive to the choice of λ and we take $\lambda = 2$

$\zeta_1^S = 20°$	$\zeta_2^S = 30°$	$\zeta_1^L = 27°$	$\zeta_2^L = 37°$
$\zeta = 21.5°$	$\mathscr{L} = 0.5$	$\alpha = 0$	$\gamma = 1.0$
$\epsilon = 0.1$	$\bar{u}_0 = 0.37822$	$\eta_0 = 0.9$	$Fr = 1.23994$
$N_x = 500$	$N_y = 500$	$CFL = 0.4$	Limiter $\theta = 1$

TABLE 1. Material parameters adopted in the numerical computations with values of the depth-averaged downslope velocity $\bar{u}_0$ and interface height η_0, which are enforced at the inflow boundary, the corresponding Froude number Fr, the number of computational grid points, N_x and N_y, in the downslope and cross-slope directions, respectively, the *CFL* number adopted in the computations, and the limiter of Jiang & Tadmor (1998) θ.

throughout. The inflow conditions (5.2) are appropriate for supercritical flows at $x = 0$, and the increase of the flow depth to the steady value ensures the flow at the inflow boundary is always supercritical. The height of the interface between the small and large particles at the inflow boundary is perturbed from the steady value η_0 by a perturbation of the form

$$\eta_p(y) = 10^{-5} \times \sin\left(\frac{2\pi y}{L_y}\right), \tag{5.3}$$

to introduce a cross-slope spatial variation. The numerical domain is taken to be sufficiently long to allow our computations to be completed before the front of flowing material approaches the boundary at $x = L_x$ so no outflow conditions are required.

Examples of the numerical solutions we obtain are shown in figures 5–7 where contours of the concentration of small particles, $\bar{\phi} = \eta/h$, the magnitude of the depth-averaged velocity, $|\bar{\boldsymbol{u}}| = \sqrt{\bar{u}^2 + \bar{v}^2}$, and the height of the layer, h, respectively, are plotted at four times. The material parameters adopted in the numerical computations, together with the computational parameters employed, are given in table 1.

The numerical solutions (figures 5–7) demonstrate the development of lobate fingers during the evolution of the flow. At early times the material propagates down the slope maintaining a uniform front (figures 5a, 6a and 7a). The flow front is predominately composed of the large material, with a sharp increase in the depth-averaged volume fraction of small material occurring behind the front. Small perturbations to the uniform front become apparent as the material propagates downslope, with the perturbations most clearly seen in the small particle concentration (figure 5b) and the velocity (figure 6b) fields. Note the wavelength of the perturbations is markedly different from the wavelength of the perturbation introduced at the inflow boundary. In those regions where the local concentration of small particles is increased, the downslope velocity is increased resulting in the formation of elongated fines-rich fingers separated by relatively slow moving regions that are enriched in the large material (see figures 5c and 6c). At later times there is a complicated interaction between the fingers with splitting and cannibalization events evident (see figures 5d and 6d). We note that these events are not visible in the height field (figure 7d) as there is little variation in the height of fines-rich fingers and the large-rich regions separating them.

While the fingers that are developed during the numerical computations appear to have a well-defined and consistent wavelength (figures 5–7), the wavelength obtained is dependent on the number of grid-points used in the computations. In figure 8 we show the contours of the depth-averaged concentration of small particles, $\bar{\phi}$, at time
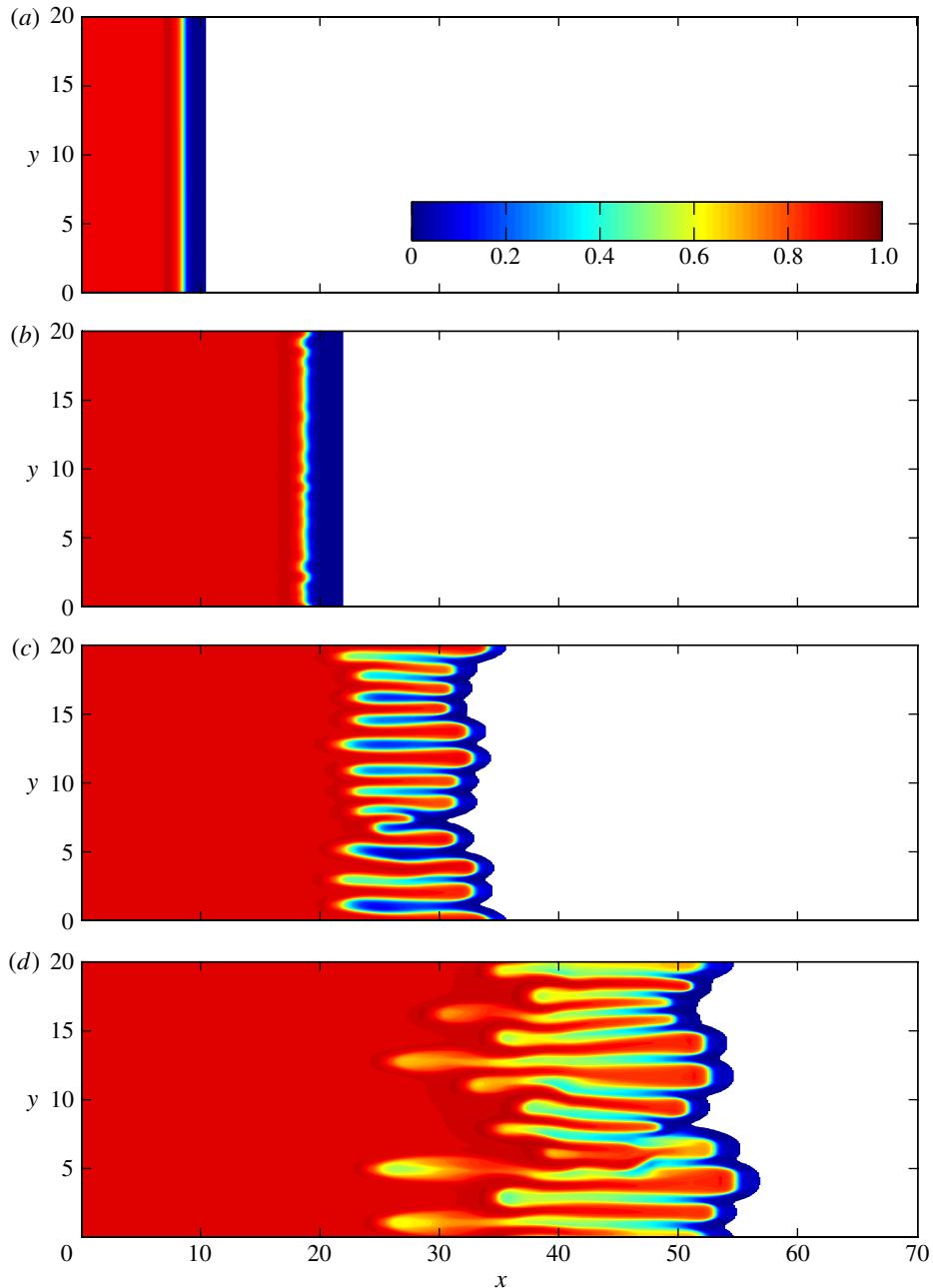
FIGURE 5. Contours of the depth-averaged concentration of small particles, $\overline{\phi} = \eta/h$, as a function of (x, y) at four instances of time, $t = 30, 78, 120$ and 195. White regions are grain free. At the inflow boundary, $x = 0$, the concentration $\overline{\phi} = 0.9$. (*a*) At early times the material propagates downslope, maintaining a uniform flow front. (*b*) The uniform flow front is unstable and perturbations develop across the front. (*c*) The small perturbations develop into a series of distinct fingers of small-rich material separated by large-rich regions. (*d*) At later times, fingers interact strongly through splitting and cannibalization. A movie showing the time-dependent simulation of this flow is available at http://dx.doi.org/10.1017/jfm.2012.348.
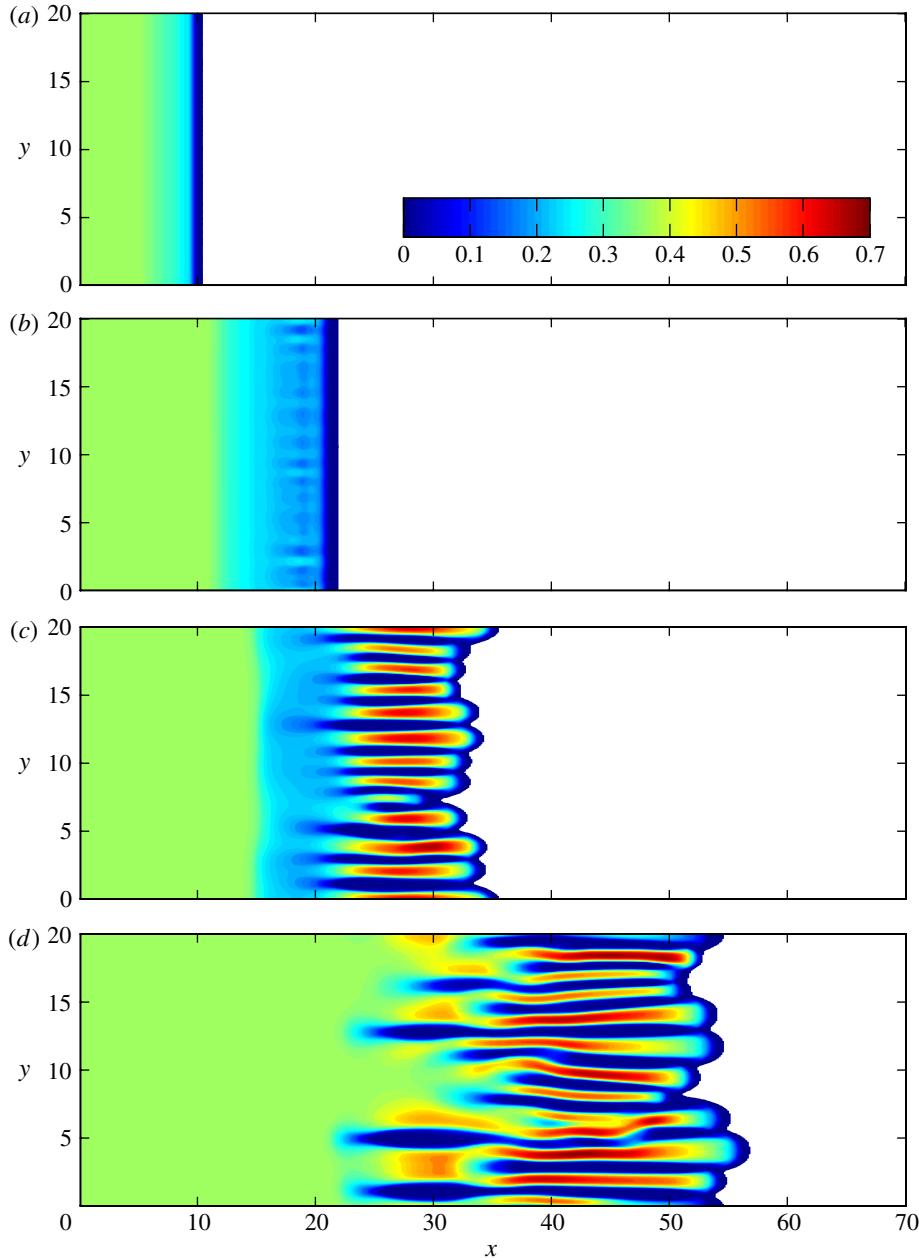
FIGURE 6. Contours of the magnitude of the depth-averaged velocity, $|\bar{\boldsymbol{u}}| = (\bar{u}^2 + \bar{v}^2)^{1/2}$, as a function of (x, y) at four instances of time, $t = 30, 78, 120$ and 195. White regions are grain free. At the inflow boundary, $x = 0$, the downslope velocity evolves rapidly to the steady velocity $\bar{u}_0$ and the cross-slope velocity $\bar{v} = 0$. (*a*) At early times the uniform flow front propagates downslope. (*b*) The instability of the front causes perturbations to the velocity field in the neighbourhood of the front. (*c,d*) As elongated fingers develop, the velocity of fines-rich material in the channels is enhanced, while the coarse-rich material separating the fingers is retarded. A movie showing the time-dependent simulation of this flow is available at http://dx.doi.org/10.1017/jfm.2012.348.
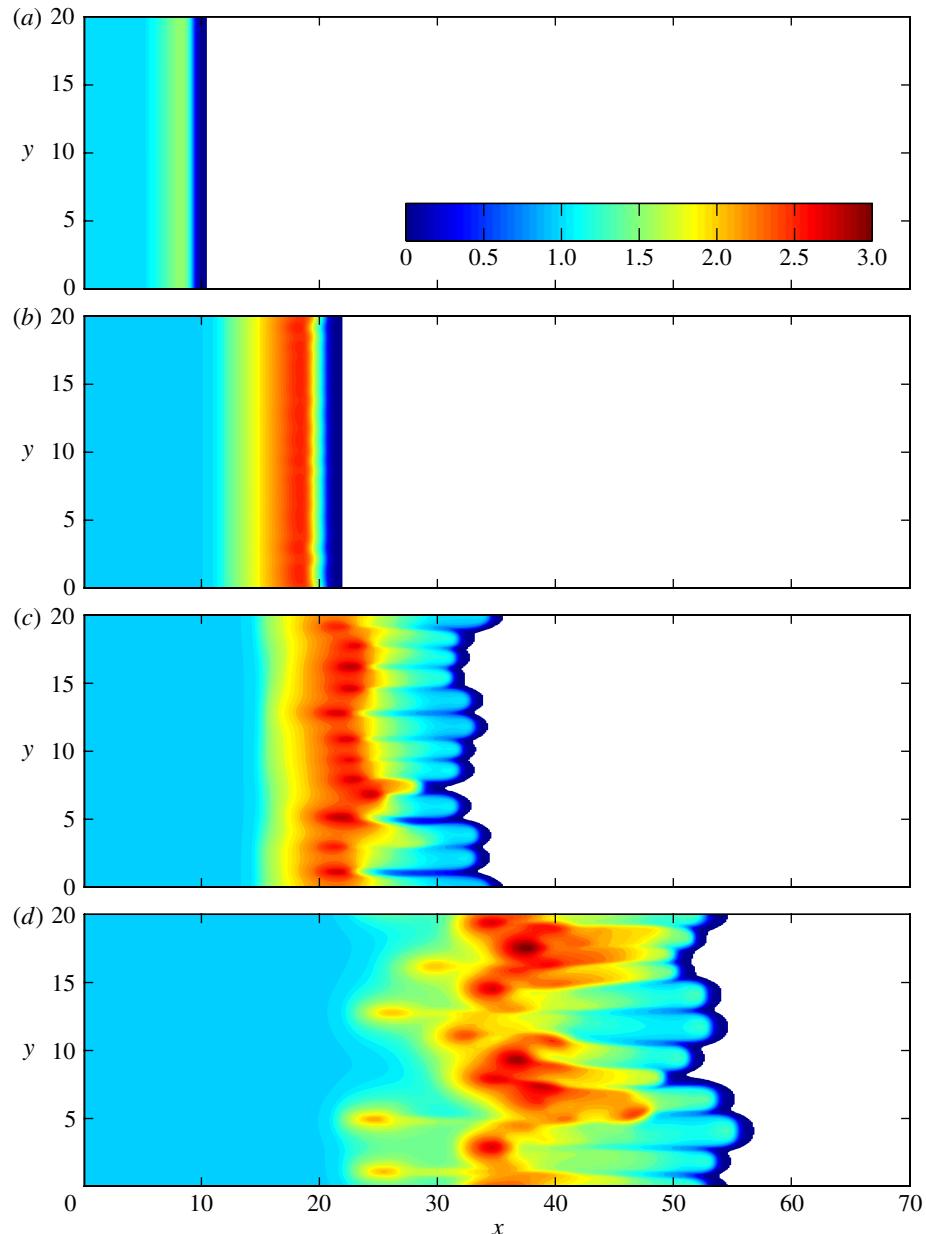
FIGURE 7. Contours of the depth of the avalanching layer, h, as a function of (x, y) at four instances of time, $t = 30, 78, 120$ and 195. White regions are grain free. At the inflow boundary, $x = 0$, the depth $h = 1$. (*a*) At early times the material propagates downslope, maintaining a uniform steep flow front. (*b*) The uniform flow front is unstable and perturbations develop across the front. (*c,d*) The small perturbations are enhanced and the front develops into a series of lobate protrusions. A movie showing the time-dependent simulation of this flow is available at http://dx.doi.org/10.1017/jfm.2012.348.
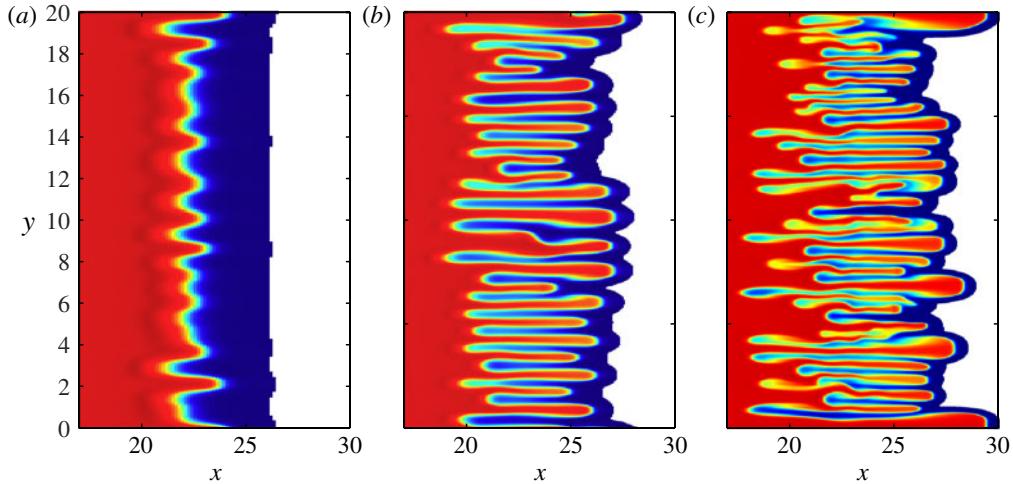
FIGURE 8. Contours of the depth-averaged concentration of small particles, $\bar{\phi} = \eta/h$, as a function of downslope, x, and cross-slope, y, position, at time $t = 90$. Three different sized computational grids (with $N_x = N_y = N$) are taken: (*a*) $N = 500$, (*b*) $N = 1000$ and (*c*) $N = 2000$. At the inflow boundary, $x = 0$, the concentration $\bar{\phi} = 0.9$.

$t = 90$ that are obtained from numerical computations which employ different numbers of grid points. The number of fines-rich fingers increases as the number of grid points increases, with the fingers becoming narrower (figure 8). As the fingers become narrower we observe more interaction between the fingers, with numerous splitting and cannibalization events (figure 8*c*). As the solutions we compute are sensitive to the number of grid points adopted in the computational scheme the numerical solutions are not able to reproduce fully the experimental observations.

The numerical computations demonstrate that the depth-averaged system of equations (4.2)–(4.5) can describe the formation of fingers following an instability of the front of the avalanche. Furthermore, the complicated interaction of fingers, once formed, can also be captured in the numerical solutions. This suggests that the system of governing equations contains sufficient physics to describe the initiation of the fingering instability and the early stages of the evolution of the fingers. However, our numerical integration of the system of equations (4.2)–(4.5) cannot produce numerically resolved fingers with a well-defined wavelength. Indeed, on refining the grid on which solutions are computed, a larger number of narrower fingers are produced. While the experimental observations show that the width of fingers are sensitive to the grain-size distribution released, the wavelength of fingers in the numerical computations are determined by the effective diffusion of the numerical scheme, with smaller diffusion at high spatial resolution giving higher-wavelength fingers. Therefore, the length scale of the fingers cannot be predicted from the numerical solutions.

6. Linear stability analysis of steady uniform flow

The numerical simulations show that the system (4.2)–(4.5) has the potential to describe finger formation through segregation-mobility feedback effects, but there is still some physics missing from the model. This is because the numerical

diffusion, which changes with grid resolution, determines the finger wavelength in the simulations. We suspect that there is a short wavelength Hadamard instability (Joseph & Saut 1990; Gray 1999), i.e. the system is ill-posed at least in some flow conditions. In order to get a precise result about the ill-posedness of the system, we focus on the problem of steady uniform flow, rather than proceeding to analyse the growth rates of the finger wavelengths at the front, which one might otherwise do. The two problems are not unrelated, since a propagating flow front has a region of steady uniform flow behind it. Therefore, if the steady uniform flow is ill-posed, it follows that the propagating flow front will be ill-posed as well.

6.1. *Linearized governing equations for small perturbations*

Small perturbations are introduced to the steady flow (4.10),

$$
\left.
\begin{aligned}
h(x, y, t) &= 1 + h_1(x, y, t), \quad \overline{u}(x, y, t) = \overline{u}_0 + \overline{u}_1(x, y, t), \\
\overline{v}(x, y, t) &= \overline{v}_1(x, y, t), \qquad \eta(x, y, t) = \eta_0 + \eta_1(x, y, t),
\end{aligned}
\right\}
\tag{6.1}
$$

with $|h_1| \ll h_0$, $|\overline{u}_1| \ll \overline{u}_0$, $|\overline{v}_1| \ll \overline{u}_0$ and $|\eta_1| \ll \eta_0$. The governing equations are linearized in the small perturbations and we obtain a linear system of partial differential equations governing the evolution of the small perturbations,

$$
\left.
\begin{aligned}
&\frac{\partial h_1}{\partial t} + \overline{u}_0 \frac{\partial h_1}{\partial x} + \frac{\partial \overline{u}_1}{\partial x} + \frac{\partial \overline{v}_1}{\partial y} = 0, \\
&\frac{\partial \overline{u}_1}{\partial t} + \overline{u}_0 \frac{\partial \overline{u}_1}{\partial x} + \epsilon \cos \zeta \frac{\partial h_1}{\partial x} = -\cos \zeta [\mu_h h_1 + \mu_u \overline{u}_1 + \mu_\eta \eta_1], \\
&\frac{\partial \overline{v}_1}{\partial t} + \overline{u}_0 \frac{\partial \overline{v}_1}{\partial x} + \epsilon \cos \zeta \frac{\partial h_1}{\partial y} = -\sin \zeta \frac{\overline{v}_1}{\overline{u}_0}, \\
&\frac{\partial \eta_1}{\partial t} + [1 - (1 - \alpha)(1 - 2\eta_0)]\overline{u}_0 \frac{\partial \eta_1}{\partial x} + [1 - (1 - \alpha)(1 - \eta_0)]\eta_0 \frac{\partial \overline{u}_1}{\partial x} \\
&\quad + [1 - (1 - \alpha)(1 - \eta_0)]\eta_0 \frac{\partial \overline{v}_1}{\partial y} - (1 - \alpha)\overline{u}_0 \eta_0{}^2 \frac{\partial h_1}{\partial x} = 0.
\end{aligned}
\right\}
\tag{6.2}
$$

The frictional interaction between the flowing layer and the stationary bed enters the linearized equations through derivatives of the friction coefficients evaluated for the steady solution,

$$
\left.
\begin{aligned}
\mu_h &= \left. \frac{\partial \mu}{\partial h} \right|_0 = (\mu_0^L - \mu_0^S)\eta_0 + \mu_h^L(1 - \eta_0) + \mu_h^S \eta_0, \\
\mu_u &= \left. \frac{\partial \mu}{\partial \overline{u}} \right|_0 = \mu_u^L(1 - \eta_0) + \mu_u^S \eta_0, \\
\mu_\eta &= \left. \frac{\partial \mu}{\partial \eta} \right|_0 = -(\mu_0^L - \mu_0^S),
\end{aligned}
\right\}
\tag{6.3}
$$

where

$$
\left.
\begin{aligned}
\mu_h^{\mathcal{N}} &= \left. \frac{\partial \mu^{\mathcal{N}}}{\partial h} \right|_0 = -\frac{3}{2}(\tan \zeta_2^{\mathcal{N}} - \tan \zeta_1^{\mathcal{N}}) \frac{\gamma e^{-\gamma/\overline{u}_0}}{\overline{u}_0}, \\
\mu_u^{\mathcal{N}} &= \left. \frac{\partial \mu^{\mathcal{N}}}{\partial \overline{u}} \right|_0 = (\tan \zeta_2^{\mathcal{N}} - \tan \zeta_1^{\mathcal{N}}) \frac{\gamma e^{-\gamma/\overline{u}_0}}{\overline{u}_0{}^2},
\end{aligned}
\right\}
\quad \text{for } \mathcal{N} = L, S,
\tag{6.4}
$$

and $\mu_0^{\mathscr{N}}$ is given by the empirical friction law (4.13). For the simple layered steady state which is perturbed, we have $\partial \mu^{\mathscr{N}}/\partial \overline{v}|_0 \equiv 0$, but we note this may not be the case for more general base states.

6.2. *Normal mode analysis*

While the resulting system of partial differential equations (6.2) is linear, an analytic solution for arbitrary initial and boundary conditions is difficult. We therefore proceed by performing a classical normal mode analysis (Drazin 1981), motivated by a formal Fourier–Laplace transform analysis of an arbitrary initial value problem in an unbounded domain. We adopt the normal mode ansatz,

$$(h_1, \overline{u}_1, \overline{v}_1, \eta_1) = (\hat{h}, \hat{u}, \hat{v}, \hat{\eta}) e^{\sigma t} e^{ik_x x + ik_y y}, \tag{6.5}$$

where (k_x, k_y) are the wavenumbers of the perturbation in the (x, y) directions, respectively, σ is the growth rate of the perturbation, and the real part of the right-hand side of (6.5) is assumed. For a temporal stability analysis the wavenumbers $(k_x, k_y) \in \mathbb{R}^2$ are imposed and the growth rate $\sigma = \sigma(k_x, k_y) \in \mathbb{C}$ is determined. If $\text{Re}(\sigma) < 0$ for all wavenumbers, then the steady flow is linearly stable as an arbitrary initial perturbation will decay exponentially quickly. However, if a wavenumber vector (k_x, k_y) can be found for which $\text{Re}(\sigma) > 0$, then the steady flow is linearly unstable and the perturbation grows exponentially quickly. If $\text{Re}(\sigma) = 0$ for all wavenumbers, then the steady flow is neutrally stable and the initial perturbation neither grows nor decays. The imaginary part of σ gives the phase speed of the perturbation. For unstable modes, if $\text{Im}(\sigma) \neq 0$ the instability is convective as an initial perturbation propagates in time, whereas a perturbation with $\text{Im}(\sigma) = 0$ is absolutely unstable as growth remains localized at the point of initiation.

On invoking the normal mode ansatz the linear system of partial differential equations is reduced to a linear system of algebraic equations,

$$\left.\begin{array}{l} \sigma \hat{h} + ik_x \overline{u}_0 \hat{h} + ik_x \hat{u} + ik_y \hat{v} = 0, \\ \sigma \hat{u} + ik_x \overline{u}_0 \hat{u} + ik_x \epsilon \cos \zeta \hat{h} = -\cos \zeta (\mu_h \hat{h} + \mu_u \hat{u} + \mu_\eta \hat{\eta}), \\ \sigma \hat{v} + ik_x \overline{u}_0 \hat{v} + ik_y \epsilon \cos \zeta \hat{h} = -\sin \zeta \hat{v}/\overline{u}_0, \\ \sigma \hat{\eta} + ik_x [1 - (1-\alpha)(1-2\eta_0)] \overline{u}_0 \hat{\eta} + ik_x [1 - (1-\alpha)(1-\eta_0)] \eta_0 \hat{u} \\ \quad + ik_y [1 - (1-\alpha)(1-\eta_0)] \eta_0 \hat{v} - ik_x (1-\alpha) \overline{u}_0 \eta_0^2 \hat{h} = 0. \end{array}\right\} \tag{6.6}$$

The algebraic system can be cast in matrix form as an eigenvalue problem in which the growth rate σ appears as the eigenvalue and the amplitudes of the normal modes are obtained as the corresponding eigenvector,

$$\boldsymbol{A}\hat{\boldsymbol{x}} = \sigma \hat{\boldsymbol{x}} \quad \text{with} \quad \hat{\boldsymbol{x}} = (\hat{h}, \hat{u}, \hat{v}, \hat{\eta})^{\text{T}}, \tag{6.7}$$

where the matrix $\boldsymbol{A}(k_x, k_y; \overline{u}_0, \eta_0)$ is a function of the underlying steady flow solution and the wavenumbers of the perturbation, and T denotes the transpose operation. The components of the matrix $\boldsymbol{A}$ are given in the Appendix. The eigenvalues are determined as the roots of the characteristic polynomial,

$$f(\sigma; k_x, k_y, \overline{u}_0, \eta_0) = \det(\sigma \boldsymbol{I} - \boldsymbol{A}) = 0, \tag{6.8}$$

where $\boldsymbol{I}$ denotes the identity. The characteristic polynomial can be found explicitly by expanding the determinant, as given in the Appendix. The growth rate is the root of the quartic polynomial f with largest real part, which we denote by σ_m.

	η_0	$\bar{u}_0$	Fr	$\bar{u}_c$
(a)	0.75	0.238	0.804	0.592
(b)	0.85	0.334	1.130	0.423
(c)	0.95	0.536	1.813	0.327
(d)	1.0	0.753	2.545	—

TABLE 2. The steady flow velocity, $\bar{u}_0$, Froude number, Fr, and critical flow velocity, $\bar{u}_c$, for the steady interface heights η_0 used in the linear stability analysis of bidisperse granular flows on a slope inclined at an angle $\zeta = 29°$. Material parameters are given in table 1. Contours of the growth rates obtained from a linear stability analysis of steady uniform flows with these parameters are shown in figure 9.

6.3. *Typical results*

For fixed controlling parameters (table 1) and a specified inclination angle ζ, a family of steady, fully developed solutions can be found by varying the interface height η_0. The steady velocity is then given by (4.14) and the range of inclination angles at which the steady solutions exist is given by (4.16). Furthermore, varying the inclination angle and interface height result in changes to the topology of the characteristic surfaces, as discussed in §4.4. Here we investigate the influence of the inclination angle and interface height on the linear stability of the steady, fully developed flow.

In figure 9 we show contours of the growth rate $\mathrm{Re}(\sigma_m)$ as a function of the downstream and cross-stream wavenumbers (k_x and k_y, respectively) for an inclination angle $\zeta = 29°$. Four different values of the interface height, η_0, are shown, which result in corresponding changes in the steady depth-averaged velocity, $\bar{u}_0$, the steady Froude number, $Fr = \bar{u}_0/\sqrt{\epsilon \cos \zeta}$, and the critical flow velocity for the steady flow, $\bar{u}_c$ defined by (4.22) (table 2). We recall that the steady flow is subcritical if $Fr < 1$ and supercritical if $Fr > 1$, and the characteristic ray Q_1 lies within the characteristic ray cone Q_s if $\bar{u}_0 < \bar{u}_c$ and lies outside the ray cone if $\bar{u}_0 > \bar{u}_c$. Note that in figure 9(d) we have taken an interface height $\eta_0 = 1.0$ corresponding to a monodisperse flow composed entirely of the small material.

Steady, fully developed bidisperse flows (shown in figure 9a–c) are linearly unstable to perturbations with $k_x > 0$ (the flows are neutrally stable for $k_x \equiv 0$, $k_y > 0$) with the exception of a region of linear stability with $k_x > 0$, $k_y > 0$ for $\eta_0 = 0.95$ (c). The growth rate increases as the downslope wavenumber k_x increases for fixed cross-stream wavenumber for each of the steady flows, except for the flow (c) where a local maxima in the growth rate occurs for a finite k_x-wavenumber for $k_y > 0$. Furthermore, for parameter sets (a) and (b) the maximum growth rate for a fixed downstream wavenumber $k_x > 0$ occurs for $k_y = 0$, indicating that purely downslope perturbations are the most rapidly growing, while for the steady flow (c) the most unstable mode occurs for $k_x > 0$, $k_y > 0$, indicating the most rapidly growing perturbations in this case are three dimensional. From table 2 we note, for the flow (c), the steady flow velocity exceeds the critical velocity, $\bar{u}_0 > \bar{u}_c$, which is in contrast to the flows (a) and (b). By further varying the steady interface height we can show that the transition from two-dimensional instability to three-dimensional instability occurs precisely when $\bar{u}_0 > \bar{u}_c$. Therefore, the topology of the characteristic conoids determines the nature of the instability of the steady, fully developed flow.
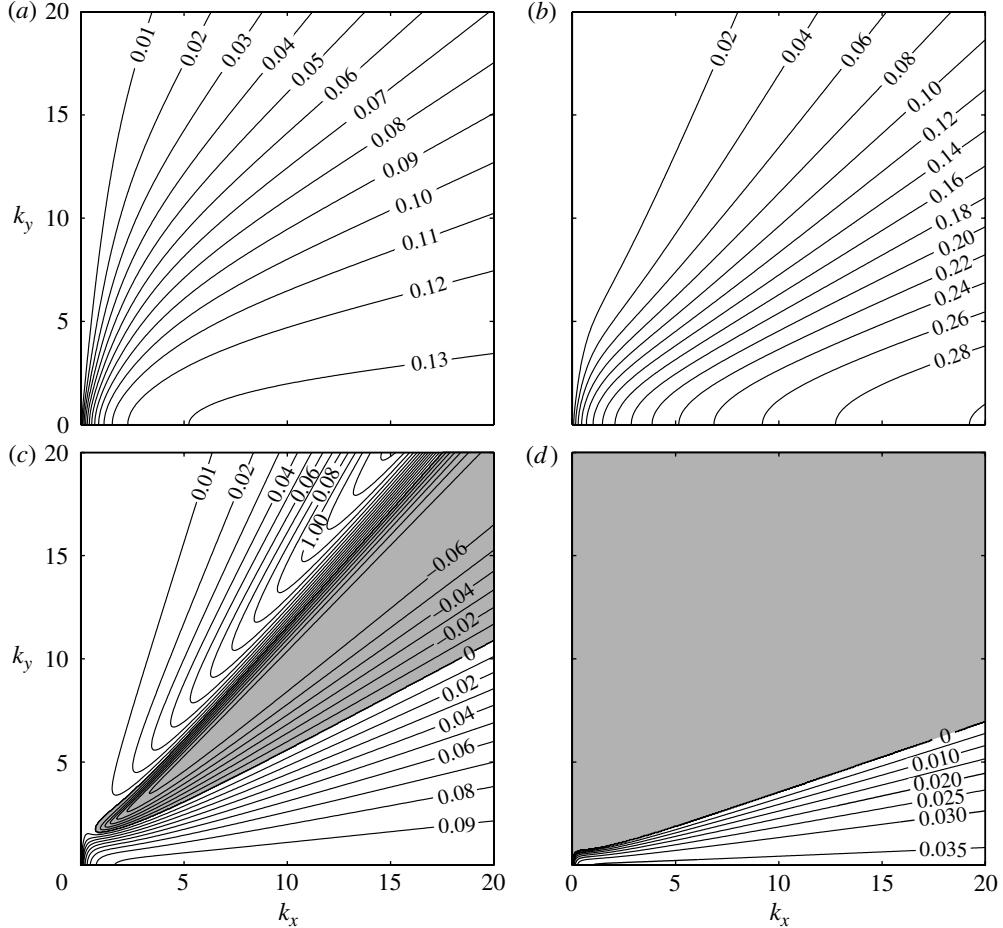
FIGURE 9. Contours of the growth rate $\text{Re}(\sigma_m)$ as a function of the wavenumbers in the downstream, k_x, and cross-stream, k_y, directions: (*a*) $\eta_0 = 0.75$ and (*b*) $\eta_0 = 0.85$ are bidisperse flows in which the most unstable mode is a purely downslope perturbation; (*c*) $\eta_0 = 0.95$ is a bidisperse flow in which the most unstable mode is a perturbation in both the downslope and cross-slope directions; (*d*) $\eta_0 = 1.0$ is a monodisperse flow. The shaded region in (*c*) marks linearly stable wavenumbers whereas the shaded region in (*d*) corresponds to neutrally stable wavenumbers. Parameters are given in table 2.

When parameters for a monodisperse flow are taken, by setting $\eta_0 = 1$ (or $\eta_0 = 0$), the topology of the dispersion relation changes, as shown in figure 9(*d*). Here there is a sharp separation (i.e. the surface is continuous but not smooth) between an unstable region and a neutrally stable region. For monodisperse flows the depth-averaged segregation equation (4.5) reduces identically to the equation for the conservation of mass (4.2). This degeneracy leads to the appearance of a neutral mode in the linear stability analysis.

The Froude number of the steady, fully developed flow can be varied by changing the inclination angle or the concentration of large particles (4.14)–(4.15). By reducing the Froude number, the influence of inertia on the flow dynamics relative to gravitational forces is reduced. Figure 10 shows the maximum growth rate, for $k_x \leqslant 20$,
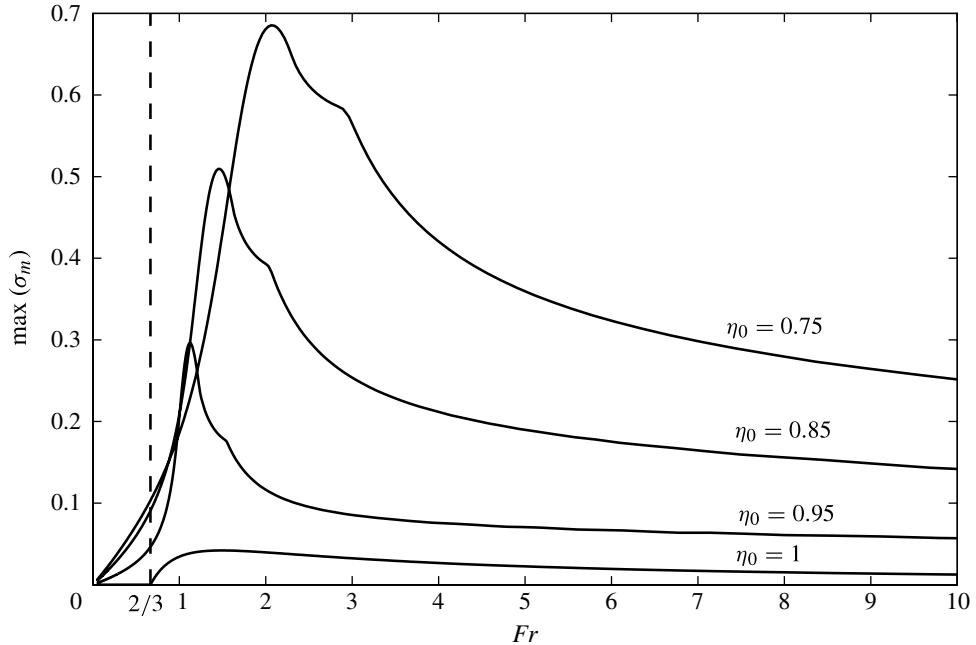
FIGURE 10. The maximum growth rate of perturbations, $\max(\sigma_m)$ for $k_x \leqslant 20$, $k_y \leqslant 20$, as a function of the steady flow Froude number, Fr. Four particle-size distributions are considered, with $\eta_0 = 0.75$, $\eta_0 = 0.85$, $\eta_0 = 0.95$, and $\eta_0 = 1$, as indicated on the figure. In the monodisperse limit $\eta \longrightarrow 1$, the linear instability of steady, fully developed flows are found for $Fr > 2/3$, while flows are neutrally stable for $Fr < 2/3$. The dashed line marks the point of transition at $Fr = 2/3$. In contrast, bidisperse flows are found to be linearly unstable for $Fr > 0$. The Froude number is varied by changing the angle of inclination, ζ. The frictional parameters of the particles are taken to be $\zeta_1^S = 20°$, $\zeta_2^S = 30°$, $\zeta_1^L = 27°$, $\zeta_2^L = 37°$, $\mathscr{L} = 0.5$, and we take $\epsilon = 0.1$ and $\alpha = 0$.

$k_y \leqslant 20$, as a function of Froude number, Fr, and interface height, η_0, for steady, fully developed flows. For bidisperse flows, $0 < \eta_0 < 1$, linear instability is found for any non-zero Froude number, suggesting the instability is not solely due to inertia. In contrast, for monodisperse flows, $\eta_0 = 0$ and $\eta_0 = 1$, there is a critical Froude number at $Fr = 2/3$ separating linearly unstable steady flows ($Fr > 2/3$) from neutrally stable steady flows ($Fr < 2/3$). This behaviour in the monodisperse limit is consistent with the results of Forterre & Pouliquen (2003) and Forterre (2006) on the spatial stability of fully developed monodisperse granular avalanches where instability was found for steady flows with $Fr > 2/3$, while steady flows with $Fr < 2/3$ were found to be linearly stable. In addition, the critical Froude number for instability of the monodisperse granular avalanche ($Fr = 2/3$) coincides with that found for roll waves on shallow liquid layers (see e.g. Whitham 1974; Needham & Merkin 1984).

To examine the role of inertia the linear stability analysis of the system has been performed with a tuning parameter ν multiplying the inertial terms in the momentum equations. For bidisperse flows, the instability persists for $\nu < 1$ and the steady flow remains linearly unstable in the limit $\nu \longrightarrow 0$. The limit $\nu \longrightarrow 0$ is the limit considered by Pouliquen & Vallance (1999), albeit for a different base flow (so the results are not directly comparable). This shows that while the effects of inertia are included in the model they are not the root cause of the instability, which is driven

by the same segregation-mobility feedback mechanism suggested by Pouliquen & Vallance (1999).

The roll wave instability of steady uniform monodisperse flows is controlled by inertia (Forterre & Pouliquen 2003; Forterre 2006). However, in contrast, the instability of bidisperse flows is not controlled by inertia. Roll wave instability has been observed in slow flows of non-Newtonian fluids (Balmforth, Bush & Craster 2005) and multicomponent systems (Balmforth, Craster & Toniolo 2003).

6.4. *High-wavenumber asymptotics*

For the system of equations (4.2)–(4.5) to be well posed we must have $\mathrm{Re}(\sigma_m)$ bounded above as $k_x \to \infty$ (Joseph & Saut 1990). We analyse the behaviour of the growth rates for large wavenumbers by performing an asymptotic analysis of the characteristic polynomial for $k_x \gg 1$.

To analyse the character of the dispersion relation for large k_x wavenumber we introduce an ordering parameter $\delta \ll 1$ and take $k_x = 1/\delta$ for a fixed $k_y \geqslant 0$. We expand the growth rate in an asymptotic series in δ, taking

$$\sigma = \delta^p (\sigma_0 + \sigma_1\delta + \cdots), \tag{6.9}$$

where the exponent, p, and the coefficients $(\sigma_0, \sigma_1, \dots)$ are to be determined. On substitution into the characteristic polynomial (6.8) we find that the distinguished limit, for which there is a balance at each order of δ, demands $p = -1$.

Expanding the characteristic polynomial for $\delta \ll 1$ we find, at order δ^{-1},

$$\begin{aligned}
f_0(\sigma_0) = \sigma_0{}^4 &+ [\mathrm{i}(4 - (1-\alpha)(1-2\eta_0))\bar{u}_0]\sigma_0{}^3 \\
&+ [\epsilon\cos\zeta - 3(2 - (1-\alpha)(1-2\eta_0))\bar{u}_0{}^2]\sigma_0{}^2 \\
&+ [\mathrm{i}(2 - (1-\alpha)(1-2\eta_0))\bar{u}_0\epsilon\cos\zeta - \mathrm{i}(4 - 3(1-\alpha)(1-2\eta_0))\bar{u}_0{}^3]\sigma_0 \\
&+ [(1 - (1-\alpha)(1-2\eta_0))\bar{u}_0{}^2(\bar{u}_0{}^2 - \epsilon\cos\zeta)] = 0. \tag{6.10}
\end{aligned}$$

The roots of this polynomial, which we denote as $\sigma_0^{(0)}$, $\sigma_0^{(1)}$, $\sigma_0^{(+)}$ and $\sigma_0^{(-)}$, are found explicitly as

$$\left.\begin{aligned}
\sigma_0^{(0)} &= -\mathrm{i}c^{(0)} \quad \text{with } c^{(0)} = \bar{u}_0, \\
\sigma_0^{(1)} &= -\mathrm{i}c^{(1)} \quad \text{with } c^{(1)} = (1 - (1-\alpha)(1-2\eta_0))\bar{u}_0, \\
\sigma_0^{(+)} &= -\mathrm{i}c^{(+)} \quad \text{with } c^{(+)} = \bar{u}_0 + \sqrt{\epsilon\cos\zeta}, \\
\sigma_0^{(-)} &= -\mathrm{i}c^{(-)} \quad \text{with } c^{(-)} = \bar{u}_0 - \sqrt{\epsilon\cos\zeta},
\end{aligned}\right\} \tag{6.11}$$

where we identify $c^{(0)}$ as the depth-averaged velocity of the steady solution, $c^{(1)}$ as the downslope velocity of the interface separating the constituent particle classes, and $c^{(+)}$ and $c^{(-)}$ are the downstream and upstream speeds, respectively, of gravity waves on the surface of the steadily flowing layer. (Note here and in the following analysis we have adopted notation which emphasizes the connection between the growth rates and wave speeds.) Thus, the eigenvalues at high k_x wavenumber are purely imaginary at leading order, indicating that the growth rate is bounded as $k_x \to \infty$ and thus the system of equations is well posed. In addition, although the phase velocity of the perturbation is unbounded as $k_x \to \infty$, the group velocity is bounded. Indeed, we note that the resulting phase speeds of the high-wavenumber perturbations are the characteristic velocities (in the downslope direction) of the linearized system of equation (6.2) (as given by (4.21)). Therefore, to leading order, the high-k_x-wavenumber perturbations are advected with the characteristic velocities.

At order 1 we obtain a linear equation for σ_1 of the form,

$$(a_3\sigma_0{}^3 + a_2\sigma_0{}^2 + a_1\sigma_0 + a_0)\sigma_1 = b_3\sigma_0{}^3 + b_2\sigma_0{}^2 + b_1\sigma_0 + b_0 \qquad (6.12)$$

where the coefficients $a_i(\bar{u}_0, \eta_0)$ and $b_i(\bar{u}_0, \eta_0)$ are given in the Appendix. On substituting the eigenvalues found at leading order, (6.11), we find

$$\left.\begin{aligned}
\sigma_1^{(0)} &= -\sin\zeta/\bar{u}_0, \\
\sigma_1^{(1)} &= -\frac{(1-\alpha)(1-\eta_0)\eta_0(1-(1-\alpha)(1-2\eta_0))\bar{u}_0(\mu_0^L - \mu_0^S)\cos\zeta}{\epsilon\cos\zeta[((1-\alpha)(1-2\eta_0)Fr)^2 - 1]}, \\
\sigma_1^{(+)} &= -\frac{(\mu_u^L(1-\eta_0) + \mu_u^S\eta_0)\epsilon\cos\zeta + (\mu_h^L(1-\eta_0) + \mu_h^S\eta_0)\sqrt{\epsilon\cos\zeta}}{2\epsilon} \\
&\quad -\frac{(1-\alpha)(1-\eta_0)\eta_0(\mu_0^L - \mu_0^S)\sqrt{\epsilon\cos\zeta}(Fr+1)}{2\epsilon[(1-\alpha)(1-2\eta_0)Fr+1]}, \\
\sigma_1^{(-)} &= -\frac{(\mu_u^L(1-\eta_0) + \mu_u^S\eta_0)\epsilon\cos\zeta - (\mu_h^L(1-\eta_0) + \mu_h^S\eta_0)\sqrt{\epsilon\cos\zeta}}{2\epsilon} \\
&\quad +\frac{(1-\alpha)(1-\eta_0)\eta_0(\mu_0^L - \mu_0^S)\sqrt{\epsilon\cos\zeta}(Fr-1)}{2\epsilon[(1-\alpha)(1-2\eta_0)Fr-1]},
\end{aligned}\right\} \qquad (6.13)$$

with the growth rate at high k_x wavenumber given by the maximum of these eigenvalues. Here $\sigma_1^{(0)}$ is obtained by substituting $\sigma_0 = \sigma_0^{(0)}$ in (6.12) and similarly for the remaining eigenvalues at order one. It is clear that $\sigma_1^{(1)} > 0$ if $|(1-\alpha)(1-2\eta_0)|Fr = \bar{u}_0/\bar{u}_c < 1$ (for $\mu_0^L > \mu_0^S$), so we have linear instability at high k_x wavenumber if the flow velocity is less than the critical velocity (4.22). The phase speed for this unstable mode, given by $\sigma_0^{(1)}$, is such that the group velocity of a wave packet coincides with the velocity of the interface. In addition, it is possible to have $\sigma_1^{(+)} > 0$ if $(1-\alpha)(1-2\eta_0)Fr < -1$, which can occur for supercritical flows ($Fr > 1$) with $\eta_0 > 1/2$ when $\bar{u}_0/\bar{u}_c > 1$. The phase speed of this unstable mode, given by $\sigma_0^{(+)}$, is such that the group velocity is the velocity of surface gravity waves. The remaining eigenvalues, $\sigma_1^{(0)}$ and $\sigma_1^{(-)}$, are negative for the material parameters we employ. We note that the leading-order growth rates at high k_x wavenumber, $\sigma_1^{(0)}$, $\sigma_1^{(1)}$, $\sigma_1^{(+)}$ and $\sigma_1^{(-)}$, are independent of the cross-slope wavenumber k_y.

On taking a monodisperse limit (i.e. either $\eta_0 \longrightarrow 0$ or $\eta_0 \longrightarrow 1$) of the growth rates (6.13) we find $\sigma_1^{(1)} \longrightarrow 0$ and

$$\sigma_1^{(\pm)} \longrightarrow -\frac{\mu_u^{\mathscr{N}}\epsilon\cos\zeta \pm \mu_h^{\mathscr{N}}\sqrt{\epsilon\cos\zeta}}{2\epsilon}, \qquad (6.14)$$

with $\mathscr{N} = L$ for $\eta_0 \longrightarrow 0$ and $\mathscr{N} = S$ for $\eta_0 \longrightarrow 1$. With the empirical form for the friction coefficient (2.6) (Pouliquen 1999a) and the partial derivatives (6.4), (6.14) can be written as

$$\sigma_1^{(\pm)} \longrightarrow -\frac{(\tan\zeta - \tan\zeta_1^{\mathscr{N}})}{2\epsilon}\frac{\gamma}{Fr}\left(\frac{1}{Fr} \mp \frac{3}{2}\right), \qquad (6.15)$$

where $\gamma > 0$ and the Froude number of the steady flow $Fr = \bar{u}_0/\sqrt{\epsilon\cos\zeta}$. Therefore, in the monodisperse limit the steady flow is linearly unstable (i.e. the growth rate is positive) at high k_x wavenumber for $Fr > 2/3$. In contrast, high-k_x-wavenumber perturbations to the steady flow are neutrally stable when $Fr < 2/3$. Furthermore, this stability condition is also obtained from numerical solution of the full dispersion relation in the monodisperse limit, as shown in figure 10. Note we do not find

linear stability for $Fr < 2/3$, as found for monodisperse roll waves by Forterre & Pouliquen (2003) and Forterre (2006), due to the neutral mode, $\sigma_1^{(1)}$, which occurs in the monodisperse limit as the large particle transport equation (4.5) reduces identically to the equation for the conservation of mass (4.2).

The high-k_x-wavenumber asymptotic expansion of the growth rates (6.9) is not appropriate when $\bar{u}_0 \longrightarrow \bar{u}_c = \sqrt{\epsilon \cos \zeta}/|(1 - \alpha)(1 - 2\eta_0)|$, where the leading-order dispersion relation at $O(1/\delta)$ is

$$
f_0(\sigma_0) = \left[\sigma_0 + \frac{i\sqrt{\epsilon \cos \zeta}}{|(1 - \alpha)(1 - 2\eta_0)|} \right] \left[\sigma_0 + i\sqrt{\epsilon \cos \zeta} \left(\frac{1}{|(1 - \alpha)(1 - 2\eta_0)|} - 1 \right) \right]
$$
$$
\times \left[\sigma_0 + i\sqrt{\epsilon \cos \zeta} \left(\frac{1}{|(1 - \alpha)(1 - 2\eta_0)|} + 1 \right) \right]
$$
$$
\times \left[\sigma_0 + i\sqrt{\epsilon \cos \zeta} \left(\frac{1}{|(1 - \alpha)(1 - 2\eta_0)|} - \frac{(1 - \alpha)(1 - 2\eta_0)}{|(1 - \alpha)(1 - 2\eta_0)|} \right) \right], \quad (6.16)
$$

and the roots are

$$
\left. \begin{aligned}
\sigma_0^{(0)} &= -\frac{i\sqrt{\epsilon \cos \zeta}}{|(1 - \alpha)(1 - 2\eta_0)|}, \\
\sigma_0^{(-)} &= -i\sqrt{\epsilon \cos \zeta} \left(\frac{1}{|(1 - \alpha)(1 - 2\eta_0)|} - 1 \right), \\
\sigma_0^{(+)} &= -i\sqrt{\epsilon \cos \zeta} \left(\frac{1}{|(1 - \alpha)(1 - 2\eta_0)|} + 1 \right),
\end{aligned} \right\} \quad (6.17)
$$

(note that $\sigma_0^{(-)}$ occurs with multiplicity 2 if $(1 - \alpha)(1 - 2\eta_0) > 0$ and $\sigma_0^{(+)}$ occurs with multiplicity 2 if $(1 - \alpha)(1 - 2\eta_0) < 0$). As there are only three distinct roots, the asymptotic expansion in the limit $\bar{u}_0 \longrightarrow \bar{u}_c$ is singular and an expansion of the roots of the form

$$
\sigma = \frac{1}{\delta}(\sigma_0 + \sigma_1 \delta^{1/2} + \sigma_2 \delta + \cdots) \quad \text{for } \delta = 1/k_x \ll 1, \quad (6.18)
$$

is required. On substitution of the series (6.18) into the dispersion relation, we find

$$
\sigma_1^{(0)} \equiv 0, \quad \sigma_2^{(0)} = -\frac{\sin \zeta |(1 - \alpha)(1 - 2\eta_0)|}{\sqrt{\epsilon \cos \zeta}}, \quad (6.19a)
$$

and, if $(1 - \alpha)(1 - 2\eta_0) > 0$,

$$
\left. \begin{aligned}
\sigma_1^{(-)} &= \pm \frac{(1 + i)}{2} \left[\frac{(1 - (1 - \alpha)(1 - 2\eta_0))}{1 - 2\eta_0}(1 - \eta_0)\eta_0 \mu_\eta \cos \zeta \right]^{1/2}, \\
\sigma_1^{(+)} &\equiv 0, \\
\sigma_2^{(+)} &= -\frac{\mu_h \cos \zeta}{2\sqrt{\epsilon \cos \zeta}} - \frac{\mu_u \cos \zeta}{2} - \frac{\eta_0 \mu_\eta \cos \zeta}{4\sqrt{\epsilon \cos \zeta}} \\
&\quad \times \left[\frac{(1 - 2\eta_0)(1 - (1 - \alpha)(1 - \eta_0)) - \eta_0}{(1 - 2\eta_0)} \right],
\end{aligned} \right\} \quad (6.19b)
$$

while, if $(1 - \alpha)(1 - 2\eta_0) < 0$,

$$
\left.
\begin{aligned}
\sigma_1^{(-)} &\equiv 0, \\
\sigma_2^{(-)} &= \frac{\mu_h \cos \zeta}{2\sqrt{\epsilon \cos \zeta}} - \frac{\mu_u \cos \zeta}{2} + \frac{\eta_0 \mu_\eta \cos \zeta}{4\sqrt{\epsilon \cos \zeta}} \\
&\quad \times \left[\frac{(1 - 2\eta_0)(1 - (1 - \alpha)(1 - \eta_0)) - \eta_0}{(1 - 2\eta_0)} \right], \\
\sigma_1^{(+)} &= \pm \frac{(1 + \mathrm{i})}{2} \left[\frac{(1 - (1 - \alpha)(1 - 2\eta_0))}{1 - 2\eta_0}(1 - \eta_0)\eta_0 \mu_\eta \cos \zeta \right]^{1/2}.
\end{aligned}
\right\}
\tag{6.19c}
$$

Therefore, if $\bar{u}_0 \longrightarrow \bar{u}_c = \sqrt{\epsilon \cos \zeta}/|(1 - \alpha)(1 - 2\eta_0)|$ the perturbation grows in time and the high-k_x-wavenumber growth rate

$$
\sigma \sim \frac{1}{2} \left[\frac{(1 - (1 - \alpha)(1 - 2\eta_0))}{1 - 2\eta_0}(1 - \eta_0)\eta_0 \mu_\eta \cos \zeta \right]^{1/2} k_x^{1/2} \quad \text{for } k_x \gg 1. \tag{6.20}
$$

The growth rate increases with increasing downslope wavenumber, indicating that small wavelength components of a perturbation are amplified more rapidly and a steady flow with $\bar{u}_0 = \bar{u}_c$ is Hadamard unstable (Joseph & Saut 1990; Goddard 2003). Therefore, if parameters are taken such that $\bar{u}_0 = \bar{u}_c$, then the system of equations (4.2)–(4.5) is ill-posed.

The high-k_x-wavenumber asymptotics show the system of equations are linearly unstable at high k_x wavenumber. For parameter choices such that $\bar{u}_0 \neq \bar{u}_c$ the growth rate of the perturbations is bounded above as $k_x \longrightarrow \infty$ so the system of equations (4.2)–(4.5) is well-posed (the system is regular in the language of Joseph & Saut (1990)), although arbitrarily small-wavelength perturbations to the steady flow grow exponentially rapidly, i.e. there is no cut-off to instability for small wavelength perturbations. We note that similar stability characteristics are found for a shallow layer of fluid on an incline, with high wavenumber modes stabilized through the inclusion of Chezy frictional resistance (Whitham 1974) and viscous dissipation (Needham & Merkin 1984). Furthermore, roll waves on a monodisperse, shallow granular layer released on an inclined plane have been observed and predicted from a linear stability analysis of a shallow-layer model of granular avalanches (Forterre & Pouliquen 2003). Here the high-wavenumber modes remain linearly unstable. However, the high-wavenumber instability can be suppressed by the inclusion of (phenomenological) viscous dissipation (Forterre 2006). It is possible that the addition of rheological terms in the equations for the conservation of momentum (4.3) and (4.4) will stabilize the small-wavelength modes.

In contrast to the linear stability of viscous fluids on an incline (Needham & Merkin 1984) or monodisperse granular avalanches (Forterre & Pouliquen 2003), our model of bidisperse granular avalanches is Hadamard unstable (Joseph & Saut 1990; Goddard 2003) on a curve in parameter space where $\bar{u}_0 \equiv \bar{u}_c$, with a growth rate $\sigma \sim k_x^{1/2}$ for $k_x \gg 1$. Thus, arbitrarily small-wavelength perturbations grow exponentially rapidly and the system of equations (4.2)–(4.5) is ill-posed in these regions of parameter space. The numerical solutions suggest that there are always points in the flow where the characteristics coincide and ill-posedness manifests itself by grid-dependent results.

7. Discussion and conclusions

Geophysical granular mass flows have polydisperse particle distributions and the different properties of the grains in the assemblage can have a pronounced effect

on the dynamics of the flows. Mathematical models of geophysical granular flows, which typically adopt a shallow-layer approach, currently do not capture the effects of the evolving particle distributions. Here, a first attempt has been made to include a description of particle-size segregation into a depth-averaged model of dense granular avalanches. Our model builds on previous theoretical models of particle-size segregation by coupling a depth-averaged description of the preferential transport of large particles to a shallow-layer model of a granular avalanche. By allowing the bulk friction coefficient of the avalanche to vary as a function of the local concentration of small particles, segregation-mobility feedback effects on the avalanche dynamics are incorporated into the avalanche model.

Numerical solutions of the governing equations we propose demonstrate that the mathematical model is able to describe the formation of a large-rich and relatively less-mobile flow front, the subsequent instability of the front and the formation of fingers bounded by large-rich levees. Furthermore, the complicated evolution of the fingers once they are formed, including merging of neighbouring fingers, cannibalization of small fingers by larger fingers, and splitting of the finger tips, which are observed in analogue laboratory experiments, is reproduced in the numerical computations. However, the numerical solutions are unable to predict the width of the fingers as the computations remain grid dependent. In §6 we show via a linear stability analysis of a steady uniform flow that the grid-dependent numerical solutions reflect an underlying pathology of the system of governing equations. In particular, for specific values of the parameters the growth rate of the instability tends to infinity with increasing wavenumber, implying that the system is Hadamard unstable and ill-posed (Joseph & Saut 1990; Goddard 2003). Therefore, while our model is able to capture several features of the formation and evolution of fingers, there are essential physical effects which are not included in the system of equations.

The short wavelength instability found in the model of bidisperse granular flows is also seen in models of monodisperse avalanches (Forterre & Pouliquen 2003), although the growth rates of high-wavenumber perturbations in the monodisperse avalanche model are bounded above (Forterre & Pouliquen 2003), so the monodisperse model is well posed. In order to stabilize short wavelengths in the monodisperse model, Forterre (2006) introduces a phenomenological viscous dissipation, based on an empirical granular rheology (GDR MiDi 2004), that provides a physical mechanism to set the wavelength of instabilities. In the bidisperse model we present, the wavelength of fingers in the numerical simulations is selected by the numerical viscosity, which changes with grid resolution. This suggests that a regularized model may be constructed by including a rheology for bidisperse granular avalanches (for example Rognon *et al.* 2007). Preliminary calculations (not shown here) suggest the inclusion of viscous terms in the system of equations (4.2)–(4.5) is sufficient to regularize the model (i.e. to obtain bounded growth rates), but not to cut-off the growth at short wavelengths. To obtain cut-off additional diffusive terms are required in the large particle transport equation. Further investigation is required to determine the physically appropriate form of both the depth-averaged rheology (which is non-unique) and also the correct form of diffusive terms in the depth-averaged description of particle-size segregation.

Supplementary movie

Supplementary movie are available at journals.cambridge.org/flm.

Appendix. Details of the linear stability analysis

The components of the 4×4 matrix $\mathbf{A}$ appearing in the eigenvalue–eigenvector problem of the linear stability analysis (6.7) are

$$A_{11} = -\mathrm{i}k_x\overline{u}_0, \quad A_{12} = -\mathrm{i}k_x, \quad A_{13} = -\mathrm{i}k_y, \quad A_{14} = 0, \tag{A 1a}$$

$$A_{21} = -\mathrm{i}k_x\epsilon\cos\zeta - \cos\zeta[(\mu_0^L - \mu_0^S)\eta_0 + \mu_h^L(1 - \eta_0) + \mu_h^S\eta_0], \tag{A 1b}$$

$$A_{22} = -\mathrm{i}k_x\overline{u}_0 - \cos\zeta[\mu_u^L(1 - \eta_0) + \mu_u^S\eta_0], \quad A_{23} = 0, \tag{A 1c}$$

$$A_{24} = \cos\zeta(\mu_0^L - \mu_0^S), \tag{A 1d}$$

$$A_{31} = -\mathrm{i}k_y\epsilon\cos\zeta, \quad A_{32} = 0, \quad A_{33} = -\mathrm{i}k_x\overline{u}_0 - \sin\zeta/\overline{u}_0, \quad A_{34} = 0, \tag{A 1e}$$

$$A_{41} = \mathrm{i}k_x(1 - \alpha)\overline{u}_0\eta_0^2, \quad A_{42} = -\mathrm{i}k_x[1 - (1 - \alpha)(1 - \eta_0)]\eta_0, \tag{A 1f}$$

$$A_{43} = -\mathrm{i}k_y[1 - (1 - \alpha)(1 - \eta_0)]\eta_0, \quad A_{44} = -\mathrm{i}k_x[1 - (1 - \alpha)(1 - 2\eta_0)]\overline{u}_0. \tag{A 1g}$$

The corresponding characteristic polynomial, $f(\sigma) = \det(\sigma\mathbf{I} - \mathbf{A})$, is a quartic polynomial which we write as $f(\sigma) = f_4\sigma^4 + f_3\sigma^3 + f_2\sigma^2 + f_1\sigma + f_0$ where the coefficients $f_i \in \mathbb{C}$ are functions of the steady solution and the wavenumbers k_x and k_y. The coefficients which define the characteristic polynomial are

$$f_4 = 1, \tag{A 2a}$$

$$f_3 = \mathrm{i}k_x[4 - (1 - \alpha)(1 - 2\eta_0)]\overline{u}_0 + \sin\zeta/\overline{u}_0 + \mu_u\cos\zeta, \tag{A 2b}$$

$$\begin{aligned} f_2 = {} & k_x^2\epsilon\cos\zeta - 3k_x^2[2 - (1 - \alpha)(1 - 2\eta_0)]\overline{u}_0^2 - \mathrm{i}k_x\mu_h\cos\zeta \\ & + \mathrm{i}k_x[3 - (1 - \alpha)(1 - 2\eta_0)]\overline{u}_0\mu_u\cos\zeta - \mathrm{i}k_x[1 - (1 - \alpha)(1 - \eta_0)]\eta_0\mu_\eta\cos\zeta \\ & + \mathrm{i}k_x[3 - (1 - \alpha)(1 - 2\eta_0)]\sin\zeta + k_y^2\epsilon\cos\zeta + \mu_u\cos\zeta\sin\zeta/\overline{u}_0, \end{aligned} \tag{A 2c}$$

$$\begin{aligned} f_1 = {} & \mathrm{i}k_x^3[2 - (1 - \alpha)(1 - 2\eta_0))\overline{u}_0\epsilon\cos\zeta - \mathrm{i}k_x^3[4 - 3(1 - \alpha)(1 - 2\eta_0)]\overline{u}_0^3 \\ & + k_x^2[2 - (1 - \alpha)(1 - 2\eta_0)]\overline{u}_0\mu_h\cos\zeta - k_x^2[3 - 2(1 - \alpha)(1 - 2\eta_0)]\overline{u}_0^2\mu_u\cos\zeta \\ & + k_x^2[2\alpha + 3(1 - \alpha)\eta_0]\eta_0\overline{u}_0\mu_\eta\cos\zeta - k_x^2(3 - 2(1 - \alpha)(1 - 2\eta_0))\overline{u}_0\sin\zeta \\ & + k_x^2\epsilon\cos\zeta\sin\zeta/\overline{u}_0 - \mathrm{i}k_x\mu_h\cos\zeta\sin\zeta/\overline{u}_0 \\ & + \mathrm{i}k_x[2 - (1 - \alpha)(1 - 2\eta_0)]\mu_u\cos\zeta\sin\zeta \\ & - \mathrm{i}k_x[1 - (1 - \alpha)(1 - \eta_0)]\eta_0\mu_\eta\cos\zeta\sin\zeta/\overline{u}_0 \\ & + \mathrm{i}k_xk_y^2[2 - (1 - \alpha)(1 - 2\eta)]\overline{u}_0\epsilon\cos\zeta + k_y^2\mu_u\cos\zeta\epsilon\cos\zeta, \end{aligned} \tag{A 2d}$$

$$\begin{aligned} f_0 = {} & k_x^4[1 - (1 - \alpha)(1 - 2\eta_0)](\overline{u}_0^2 - \epsilon\cos\zeta)\overline{u}_0^2 \\ & + \mathrm{i}k_x^3[1 - (1 - \alpha)(1 - 2\eta_0)]\overline{u}_0^2(\mu_h - \overline{u}_0\mu_u + \eta_0\mu_\eta)\cos\zeta \\ & - \mathrm{i}k_x^3[1 - (1 - \alpha)(1 - 2\eta_0)](\overline{u}_0^2 - \epsilon\cos\zeta)\sin\zeta \\ & + k_x^2[1 - (1 - \alpha)(1 - 2\eta_0)](\mu_h - \overline{u}_0\mu_u + \eta_0\mu_\eta)\cos\zeta\sin\zeta \end{aligned}$$

$$- k_x{}^2 k_y{}^2 [1 - (1 - \alpha)(1 - 2\eta_0)]\bar{u}_0{}^2 \epsilon \cos \zeta$$

$$+ \mathrm{i} k_x k_y{}^2 [1 - (1 - \alpha)(1 - 2\eta_0)]\bar{u}_0 \mu_u \cos \zeta \epsilon \cos \zeta. \qquad (\mathrm{A}\,2e)$$

The coefficients in the linear equation (6.12) determining σ_1 are

$$a_3 = 4, \qquad (\mathrm{A}\,3a)$$

$$a_2 = 3\mathrm{i}[4 - (1 - \alpha)(1 - 2\eta_0)]\bar{u}_0, \qquad (\mathrm{A}\,3b)$$

$$a_1 = 2\epsilon \cos \zeta - 6[2 - (1 - \alpha)(1 - 2\eta_0)]\bar{u}_0{}^2, \qquad (\mathrm{A}\,3c)$$

$$a_0 = \mathrm{i}[2 - (1 - \alpha)(1 - 2\eta_0)]\epsilon \cos \zeta \bar{u}_0 - \mathrm{i}[4 - 3(1 - \alpha)(1 - 2\eta_0)]\bar{u}_0{}^3, \qquad (\mathrm{A}\,3d)$$

$$b_3 = [\mu_u^L(1 - \eta_0) + \mu_u^S \eta_0] \cos \zeta + \sin \zeta / \bar{u}_0, \qquad (\mathrm{A}\,3e)$$

$$b_2 = \mathrm{i}[3 - (1 - \alpha)(1 - 2\eta_0)][\mu_u^L(1 - \eta_0) + \mu_u^S \eta_0] \cos \zeta \bar{u}_0 + \mathrm{i}[3 - (1 - \alpha)(1 - 2\eta_0)] \sin \zeta$$

$$\qquad + \mathrm{i}(1 - \alpha)(1 - \eta_0)\eta_0(\mu_0^L - \mu_0^S) \cos \zeta - \mathrm{i}[\mu_h^L(1 - \eta_0) + \mu_h^S \eta_0] \cos \zeta, \qquad (\mathrm{A}\,3f)$$

$$b_1 = -[3 - 2(1 - \alpha)(1 - 2\eta_0)][\mu_u^L(1 - \eta_0) + \mu_u^S \eta_0] \cos \zeta \bar{u}_0{}^2$$

$$\qquad + (1 - \alpha)(1 - \eta_0)\eta_0(\mu_0^L - \mu_0^S) \cos \zeta \bar{u}_0 - [3 - 2(1 - \alpha)(1 - 2\eta_0)] \sin \zeta \bar{u}_0$$

$$\qquad + [2 - (1 - \alpha)(1 - 2\eta_0)][\mu_h^L(1 - \eta_0) + \mu_h^S \eta_0] \cos \zeta \bar{u}_0 + \epsilon \cos \zeta \sin \zeta / \bar{u}_0, \qquad (\mathrm{A}\,3g)$$

$$b_0 = -\mathrm{i}[1 - (1 - \alpha)(1 - 2\eta_0)]\{[\mu_u^L(1 - \eta_0) + \mu_u^S \eta_0] \cos \zeta \bar{u}_0{}^3 + \sin \zeta \bar{u}_0{}^2$$

$$\qquad - [\mu_h^L(1 - \eta_0) + \mu_h^S \eta_0] \cos \zeta \bar{u}_0{}^2 - \epsilon \cos \zeta \sin \zeta\}. \qquad (\mathrm{A}\,3h)$$

REFERENCES

ABRAMOWITZ, M. & STEGUN, I. 1970 *Handbook of Mathematical Functions*, 9th edn. p. 3.3.7. Dover.

BALMFORTH, N. J., BUSH, J. W. M. & CRASTER, R. V. 2005 Roll waves on flowing cornstarch suspensions. *Phys. Lett.* A **338**, 479–484.

BALMFORTH, N. J., CRASTER, R. V. & TONIOLO, C. 2003 Interfacial instability in non-Newtonian fluid layers. *Phys. Fluids* **15**, 3370.

BRANNEY, M. J. & KOKELAAR, P. 2002 *Pyroclastic Density Currents and the Sedimentation of Ignimbrites. Memoirs, vol. 27*, Geological Society.

COOKE, M. H., STEPHENS, D. J. & BRIDGWATER, J. 1976 Powder mixing – a literature survey. *Powder Tech.* **15** (1), 1–20.

COURANT, R. & HILBERT, D. 1962 *Methods of Mathematical Physics*, 1st edn. *Differential Equations, vol. II*, Wiley.

CUI, X., GRAY, J. M. N. T. & JÓHANNESSON, T. 2007 Deflecting dams and the formation of oblique shocks in snow avalanches at Flateyri, Iceland. *J. Geophys. Res.* **112**, F04012.

DALBEY, K., PATRA, A. K., PITMAN, E. B., BURSIK, M. I. & SHERIDAN, M. F. 2008 Input uncertainty propagation methods and hazard mapping of geophysical mass flows. *J. Geophys. Res.* **113**, B05203.

DENLINGER, R. P. & IVERSON, R. M. 2001 Flow of variably fluidized granular masses across three-dimensional terrain. 2. Numerical predictions and experimental tests. *J. Geophys. Res.* **106** (B1), 553–566.

DOLGUNIN, V. N. & UKOLOV, A. A. 1995 Segregation modelling of particle rapid gravity flow. *Powder Tech.* **83** (2), 95–103.

DOYLE, E. E., HOGG, A. J., MADER, H. M. & SPARKS, R. S. J. 2008 Modelling dense pyroclastic basal flows from collapsing columns. *Geophys. Res. Lett.* **35**, L04305.

DRAZIN, P. G. 1981 *Hydrodynamic Stability*, 1st edn. Cambridge University Press.

FÉLIX, G. & THOMAS, N. 2004 Relation between dry granular flow regimes and morphology of deposits: formation of levées in pyroclastic deposits. *Earth Planet. Sci. Lett.* **221**, 197–213.

FORTERRE, Y. 2006 Kapiza waves as a test for three-dimensional granular flow rheology. *J. Fluid Mech.* **563**, 123–132.

FORTERRE, Y. & POULIQUEN, O. 2003 Long-surface-wave instability in dense granular flows. *J. Fluid Mech.* **486**, 21–50.

FORTERRE, Y. & POULIQUEN, O. 2008 Flows of dense granular media. *Annu. Rev. Fluid Mech.* **40**, 1–24.

GDR MiDi, 2004 On dense granular flows. *Eur. Phys. J.* E **14** (4), 341–365.

GODDARD, J. D. 2003 Material instability in complex fluids. *Annu. Rev. Fluid Mech.* **35**, 113–133.

GOLICK, L. A. & DANIELS, K. E. 2009 Mixing and segregation rates in sheared granular materials. *Phys. Rev.* E **80**, 042301.

GOUJON, C., DALLOZ-DUBRUJEAUD, B. & THOMAS, N. 2007 Bidisperse granular avalanches on inlined planes: a rich variety of behaviours. *Eur. Phys. J.* E **23** (2), 199–215.

GRAY, J. M. N. T. 1999 Loss of hyperbolicity and ill-posedness of the viscous-plastic sea ice rheology in uniaxial divergent flow. *J. Phys. Oceanogr.* **29**, 2920–2929.

GRAY, J. M. N. T. & ANCEY, C. 2009 Segregation, recirculation and deposition of coarse particles near two-dimensional avalanche fronts. *J. Fluid Mech.* **629**, 387–423.

GRAY, J. M. N. T. & ANCEY, C. 2011 Multi-component particle-size segregation in shallow granular avalanches. *J. Fluid Mech.* **678**, 535–588.

GRAY, J. M. N. T. & CHUGUNOV, V. A. 2006 Particle-size segregation and diffusive remixing in shallow granular avalanches. *J. Fluid Mech.* **569**, 365–398.

GRAY, J. M. N. T. & CUI, X. 2007 Weak, strong and detached oblique shocks in gravity-driven granular free-surface flows. *J. Fluid Mech.* **579**, 113–136.

GRAY, J. M. N. T. & HUTTER, K. 1997 Pattern formation in granular avalanches. *Contin. Mech. Thermodyn.* **9** (6), 341–345.

GRAY, J. M. N. T. & KOKELAAR, B. P. 2010a Large particle segregation, transport and accumulation in granular free-surface flows. *J. Fluid Mech.* **652**, 105–137.

GRAY, J. M. N. T. & KOKELAAR, B. P. 2010b Large particle segregation, transport and accumulation in granular free-surface flows – erratum. *J. Fluid Mech.* **657**, 539.

GRAY, J. M. N. T., SHEARER, M. & THORNTON, A. R. 2006 Time-dependent solution for particle-size segregation in shallow granular avalanches. *Proc. R. Soc.* A **462** (2067), 947–972.

GRAY, J. M. N. T., TAI, Y.-C. & NOELLE, S. 2003 Shock waves, dead zones and particle-free regions in rapid granular free-surface flows. *J. Fluid Mech.* **491**, 161–181.

GRAY, J. M. N. T. & THORNTON, A. R. 2005 A theory for particle size segregation in shallow granular free-surface flows. *Proc. R. Soc.* A **461** (2057), 1447–1473.

GRAY, J. M. N. T., WIELAND, M. & HUTTER, K. 1999 Gravity-driven free surface flow of granular avalanches over complex basal topography. *Proc. R. Soc.* A **455** (1985), 1841–1874.

GRUBER, U. & BARTELT, P. 2007 Snow avalanche hazard modelling of large areas using shallow water numerical methods and GIS. *Environ. Modell. Softw.* **22** (10), 1472–1481.

HÁKONARDÓTTIR, K. M. & HOGG, A. J. 2005 Oblique shocks in rapid granular flows. *Phys. Fluids* **17** (7), 077101.

IVERSON, R. M. 1997 The physics of debris flows. *Rev. Geophys.* **35** (3), 245–296.

IVERSON, R. M. 2003 The debris-flow rheology myth. In *Debris-Flow Hazards Mitigation: Mechanics, Prediction, and Assessment* (ed. D. Rickenmann & C.L. Chen). pp. 303–314. Millpress.

IVERSON, R. M. & DENLINGER, R. P. 2001 Flow of variably fluidized granular masses across three-dimensional terrain. 1. Coulomb mixture theory. *J. Geophys. Res.* **106** (B1), 537–552.

IVERSON, R. M. & VALLANCE, J. W. 2001 New views of granular mass flows. *Geology* **29** (2), 115–118.

JIANG, G.-S. & TADMOR, E. 1998 Nonoscillatory centre schemes for multidimensional hyperbolic conservation laws. *SIAM J. Sci. Comput.* **19** (6), 1892–1917.

JOHNSON, C. G. & GRAY, J. M. N. T. 2011 Granular jets and hydraulic jumps on an inclined plane. *J. Fluid Mech.* **675**, 87–116.

JOHNSON, C. G., KOKELAAR, B. P., IVERSON, R. M., LOGAN, M., LaHUSEN, R. G. & GRAY, J. M. N. T. 2012 Grain-size segregation and levee formation in geophysical mass flows. *J. Geophys. Res.* **117**, F01032.

JOP, P., FORTERRE, Y. & POULIQUEN, O. 2006 A constitutive relation for dense granular flows. *Nature* **44**, 727–730.

JOSEPH, D. D. & SAUT, J. C. 1990 Short-wave instabilities and ill-posed initial-value problems. *Theor. Comput. Fluid Dyn.* **1**, 191–227.

LUBE, G., CRONIN, S. J., PLATZ, T., FREUNDT, A., PROCTER, J. N., HENDERSON, C. & SHERIDAN, M. F. 2007 Flow and deposition of pyroclastic granular flows: a type example from the 1975 Ngauruhoe eruption, New Zealand. *J. Volcanol. Geotherm. Res.* **161**, 165–186.

MANGENEY, A., BOUCHUT, F., THOMAS, N., VILOTTE, J. P. & BRISTEAU, M. O. 2007 Numerical modelling of self-channeling granular flows and of their levee-channel deposits. *J. Geophys. Res.* **112**, F02017.

MAY, L. B. H., GOLICK, L. A., PHILLIPS, K. C., SHEARER, M. & DANIELS, K. E. 2010 Shear-driven size segregation of granular materials: modelling and experiment. *Phys. Rev.* E **81**, 051301.

McINTYRE, M., ROWE, E. L., SHEARER, M., GRAY, J. M. N. T. & THORNTON, A. R. 2008 Evolution of a mixing zone in granular avalanches. *Appl. Math. Res. Express* **2008**, 1–12.

MIDDLETON, G. V. 1970 Experimental studies related to problems of flysch sedimentation. In *Flysch Sedimentology in North America* (ed. J. Lajoie). pp. 253–272. Geol. Assoc. Can. Spec. Pap. 7.

MORLAND, L. W. 1992 Flow of viscous fluid through a porous deformable matrix. *Surv. Geophys.* **13** (3), 209–268.

NEEDHAM, D. J. & MERKIN, J. H. 1984 On roll waves down an open inclined channel. *Proc. R. Soc. Lond.* A **394**, 259–278.

OTTINO, J. M. & KHAKHAR, D. V. 2000 Mixing and segregation of granular materials. *Annu. Rev. Fluid Mech.* **32**, 55–91.

PHILLIPS, J. C., HOGG, A. J., KERSWELL, R. R. & THOMAS, N. H. 2006 Enhanced mobility of granular mixtures of fine and coarse particles. *Earth Planet. Sci. Lett.* **246** (3-4), 466–480.

PIERSON, T. C. 1986 Flow behaviour of channelized debris flows, Mount St. Helens, Washington. In *Hillslope Processes* (ed. A.D. Abrahams). pp. 269–296. Allen and Unwin.

PITMAN, E. B., NICHITA, C. C., PATRA, A., BAUER, A., SHERIDAN, M. & BURSIK, M. 2003 Computing granular avalanches and landslides. *Phys. Fluids* **15** (12), 3638–3646.

POULIQUEN, O. 1999a Scaling laws in granular flows down rough inclined planes. *Phys. Fluids* **11** (3), 542–548.

POULIQUEN, O. 1999b On the shape of granular fronts down rough inclined planes. *Phys. Fluids* **11** (7), 1956–1958.

POULIQUEN, O., DELOUR, J. & SAVAGE, S. B. 1997 Fingering in granular flows. *Nature* **386**, 816–817.

POULIQUEN, O. & VALLANCE, J. W. 1999 Segregation induced instabilities of granular fronts. *Chaos* **9** (3), 621–630.

REYNOLDS, O. 1885 On the dilatancy of media composed of rigid particles in contact. With experimental illustrations. *Phil. Mag. Ser. 5* **20** (127), 469–481.

ROGNON, P. G., ROUX, J.-N., NAAÏM, M. & CHEVOIR, F. 2007 Dense flows of bidisperse assemblies of disks down an inclined plane. *Phys. Fluids* **19**, 058101.

SAVAGE, S. B. & HUTTER, K. 1989 The motion of a finite mass of granular material down a rough incline. *J. Fluid Mech.* **199**, 177–215.

SAVAGE, S. B. & LUN, C. K. K. 1988 Particle size segregation in inclined chute flow of dry cohesionless granular solids. *J. Fluid Mech.* **189**, 311–335.

SHEARER, M., GRAY, J. M. N. T. & THORNTON, A. R. 2008 Stable solutions of a scalar conservation law for particle-size segregation in dense granular avalanches. *Eur. J. Appl. Maths* **19** (1), 61–86.

THORNTON, A. R. & GRAY, J. M. N. T. 2008 Breaking size segregation waves and particle recirculation in granular avalanches. *J. Fluid Mech.* **596**, 261–284.

THORNTON, A. R., GRAY, J. M. N. T. & HOGG, A. J. 2006 A three-phase mixture theory for particle size segregation in shallow granular free-surface flows. *J. Fluid Mech.* **550**, 1–25.

TRUESDELL, C. 1984 *Rational Thermodynamics*. Springer.

VALLANCE, J. W. & SAVAGE, S. B. 2000 Particle segregation in granular flows down chutes. In *IUTAM Symposium on Segregation in Granular Flows* (ed. A.D. Rosato & D.L. Blackmore). pp. 31–51. Kluwer.

VREMAN, A. W., AL-TARAZI, M., KUIPERS, A. M., VAN SINT ANNALAND, M. & BOKHOVE, O. 2007 Supercritical shallow granular flow through a contraction: experiment, theory and simulation. *J. Fluid Mech.* **578**, 233–269.

WEIYAN, T. 1992 *Shallow Water Hydrodynamics*. Elsevier.

WHITHAM, G. B. 1974 *Linear and Nonlinear Waves*. Wiley.

WIEDERSEINER, S., ANDREINI, N., ÉPEL-CHAUVIN, G., MOSER, G., MONNEREAU, M., GRAY, J. M. N. T. & ANCEY, C. 2011 Experimental investigation into segregating granular flows down chutes. *Phys. Fluids* **23**, 013301.

WILLIAMS, R., STINTON, A. J. & SHERIDAN, M. F. 2008 Evaluation of the Titan2D two-phase flow model using an actual event: case study of the 2005 Vazcún Valley Lahar. *J. Volcanol. Geotherm. Res.* **177** (4), 760–766.